

## Accurate modeling of photovoltaic modules using a 1-D deep residual network based on I-V characteristics

Zhicong Chen<sup>a,b</sup>, Yixiang Chen<sup>a,b</sup>, Lijun Wu<sup>a,b,\*</sup>, Shuying Cheng<sup>a,b,\*</sup>, Peijie Lin<sup>a,b</sup>, Linlin You<sup>c</sup>

<sup>a</sup> College of Physics and Information Engineering, Fuzhou University, 2 XueYuan Road, 350116 Fuzhou, China

<sup>b</sup> Jiangsu Collaborative Innovation Centre of Photovoltaic Science and Engineering, 213164 Changzhou, China

<sup>c</sup> Future Urban Mobility Interdisciplinary Research Group, Singapore-MIT Alliance for Research and Technology Centre, #09-02, 1 CREATE Way, 138602 Singapore, Singapore

### ARTICLE INFO

#### Keywords:

Photovoltaic modeling  
Black-box modeling  
I-V characteristic prediction  
Deep learning  
Convolutional neural network  
Deep residual network

### ABSTRACT

Accurate and reliable modeling of photovoltaic (PV) modules is significant for optimal design, operation and evaluation of PV systems. PV models can be classified into equivalent circuit-based white box models and data-driven black box models. Due to the difficulty to obtain the ground true model parameters and the limitation posed by the predetermined model structure, white-box modeling methods generally suffer relatively low accuracy and generalization performance for arbitrary operating conditions. In addition, reported black-box models are based on the conventional artificial neural networks (ANN) that are efficient but have limited performance. In this study, motivated by the high performance of fast developing deep learning techniques, we propose a novel black-box modeling method for the PV modules using a new modified one-dimensional deep residual network (1-D ResNet) and measured I-V characteristic curves, which can predict a whole I-V curve at a time for arbitrary operating conditions. To alleviate the overfitting issue caused by imbalanced data, original I-V curve datasets with highly non-uniform operating conditions are resampled by a grid sampling approach to obtain the datasets with relatively uniform conditions for the subsequent modeling. The proposed 1-D ResNet based model is comprehensively verified and compared with a proposed single-diode based white-box model and three other conventional ANN based black-box models, using large datasets of measured I-V characteristic curves from the National Renewable Energy Laboratory (NREL). Experimental results indicate that black-box models are generally better than the white-box model. Especially, the proposed 1-D ResNet based PV model is obviously superior to other three conventional ANN based black-box models, in terms of accuracy, generalization performance and reliability.

### 1. Introduction

To address increasingly serious energy crisis and environmental pollution issues, solar energy has emerged as an important kind of new energy sources, because of the cleanness, sustainability and broad availability. According to the report of the international energy agency (IEA), the PV installed capacity has been undergoing rapid increase in recent years [1]. As the fundamental energy harvesting components of PV systems, accurate and reliable modeling of the PV modules and arrays is important and significant for optimal simulation, design, operation and evaluation of PV systems [2–4], such as maximum power point tracking (MPPT) [5], power forecasting [6], fault detection and diagnosis [7–11], and so on. Usually, manufacturers provide some rated electrical parameters of PV modules to support the modeling and power calculation, including open-circuit voltage, short-circuit current,

maximum power point voltage and current, and temperature coefficients and so on. However, the rated data are initially accurate at standard test condition (STC), but PV modules inevitably suffer degradation in real long term operation. Therefore, **current-voltage (I-V) characteristic data measured in field under operating conditions (OPC)** are more appropriate for accurate PV modelling, based on which many PV modeling approaches were proposed in recent years [3,12–15]. These approaches could be generally classified into two categories: equivalent circuit based **white-box models** [12,13,16–19] and regression based **black-box models** [3,20,21].

The white-box PV modeling needs to first determine an equivalent circuit and then identify the model parameters from the measured I-V characteristics. PV modules/arrays are composed of many solar cells connected in series and/or in parallel, while a solar cell fundamentally is a P-N junction diode that converts light into current according to the

\* Corresponding authors at: College of Physics and Information Engineering, Fuzhou University, 2 XueYuan Road, 350116 Fuzhou, China.

E-mail addresses: [lijun.wu@fzu.edu.cn](mailto:lijun.wu@fzu.edu.cn) (L. Wu), [sycheng@fzu.edu.cn](mailto:sycheng@fzu.edu.cn) (S. Cheng).

<b>Nomenclature</b>	
<i>Abbreviations</i>	
ABC	artificial bee colony
AC	alternating current
Adam	adaptive moment estimation
ANN	artificial neural networks
BPNN	back-propagation neural network
CNN	convolutional neural networks
CPV	concentrator photovoltaic
DC	direct current
DNN	deep neural networks
EHA-NMS	eagle strategy based hybrid adaptive Nelder-Mead simplex algorithm
ELM	extreme learning machine
FC	fully connected
GRNN	generalized regression neural network
IEA	international energy agency
I-V	current-voltage
MLP	multi-layer perceptron machine
MPP	maximum power point
MIMO	multi-input multi-output
MPP	maximum power points
MPPT	maximum power point tracking
MSE	mean square error
NMS	Nelder-Mead simplex
NREL	national renewable energy laboratory
nRMSE	normalized root mean square error
OPC	operating condition
POA	plane-of-array
PV	photovoltaic
RBFNN	radial basis function neural network
RMSE	root mean square error
SGD	stochastic gradient descent
SISO	single-input single-output
STC	standard test condition
1-D ResNet	one-dimensional deep residual network
<i>Symbols</i>	
$\alpha$	temperature coefficient
$\beta$	irradiance coefficient
$E_g$	energy band gap
$G$	irradiance ( $\text{W}/\text{m}^2$ )
$G_{STC}$	irradiance in STC ( $\text{W}/\text{m}^2$ )
$I_o$	output PV current (A)
$I_{pv}$	photocurrent (A)
$I_{pv,STC}$	photocurrent in STC (A)
$K$	Boltzmann constant (J/K)
$M_p$	number of solar cell strings connected in parallel
$M_s$	number of solar cells in series in a string
$n$	diode ideality factor
$n_{STC}$	diode ideality factor in STC
$q$	charge of one electron (C)
$R_s$	series resistance ( $\Omega$ )
$R_{sh}$	shunt resistance ( $\Omega$ )
$T$	absolute temperature of a solar cell (K)
$T_{STC}$	absolute temperature in STC (K)

photoelectric effect. Therefore, all of equivalent-circuit based white-box PV models include a current source and a diode at least. In the literature, there are various equivalent circuit models for solar cells/PV modules/PV arrays [2], including ideal single-diode model with 3 parameters [2], single-diode  $R_s$  model with 4 parameters [2], single-diode  $R_p$  model with 5 parameters [12,13], double-diode model with 7 parameters [16,18,19,22–24], and dynamic model with 4 static parameters and 3 dynamic parameters [25]. The ideal single-diode model was modeled as a current source with a reverse diode in parallel [2,26]. The single-diode  $R_s$  model improve the ideal model by taking in account a series resistor  $R_s$  to model the loss due to contact resistances between the electrodes and silicon [27], while the single-diode  $R_p$  model incorporates one more shunt resistor  $R_p$  to simulate the leakage current of P-N junction [2]. However, single-diode models neglect the recombination loss occurring in depletion region, which limits the model accuracy. Taking into the recombination effect, double-diode models were proposed, which include one more diode and exhibit higher accuracy in comparison to the single-diode  $R_p$  model [22]. The aforementioned models are static and achieve good trade-off between the simplicity and accuracy, but they cannot reflect the dynamic characteristic under dynamic load. Thus, based the static models, dynamic models were proposed as well, which further incorporate capacitors and/or inductors [28]. Once the equivalent circuits are determined, parameter identification should be performed based on I-V characteristic data. Therefore, various parameter estimation techniques were proposed accordingly [29,30], including analytic methods [31,32], numerical methods [23,33,34], and hybrid methods [19,35,36]. Most of these methods extract the parameters by curve fitting (i.e., by minimizing the deviation between the measured and calculated I-V curves or some key points). Therefore, the extracted parameters are sensitive to noise and accuracy of measured I-V curves and are not guaranteed to be the ground true. In addition, these parameter extraction techniques only can identify model parameters at a specific

operating condition. In order to obtain a complete PV model for arbitrary operating conditions, the relationship equations between model parameters and operating temperature and irradiance should be further determined and calibrated [30,32,37]. Therefore, the performance of white box PV models is greatly affected and limited by model equivalent circuits, the relationship equation of parameters with respect to the irradiance and temperature, and the quality of the measured I-V curves.

In contrast to equivalent circuit based white-box PV modeling techniques, data-driven black-box PV modeling techniques directly build PV models from measured data by regression and need no any predetermined equivalent circuits and parameter equations with respect to operating conditions, which can avoid the drawbacks of white-box models and thus are usually more accurate and general [3,38]. In the literature, various conventional artificial neural networks (ANN) have been applied to perform regression based PV modeling by automatically learning the complex nonlinear mapping relationship between inputs and outputs, including single-layer back-propagation neural network (BPNN) [39,40], multi-layer BPNN [41], generalized regression neural network (GRNN) [42,43], radial basis function neural network (RBFNN) [44], multi-layer perceptron (MLP) neural networks [45–48], extreme learning machine (ELM) [49], and so on. Although the aforementioned conventional ANN based models achieve good tradeoff between the accuracy and the simplicity, their accuracy and generalization performance are still limited, because of that PV models feature a highly non-linear and complex relationship with respect to ambient conditions. With the fast development of the microprocessor technologies, computing capability of common computers and/or embedded devices are rapidly increasing, which support much more complex ANN that contribute a higher accuracy and performance. In recent years, deep learning based deep neural networks (DNN) have emerged as powerful machine learning tools that enable complicated pattern recognition and regression analysis or prediction applications [50,51]. Essentially, DNN is a class of ANN with multiple layers

between input and output layers, and it is powerful at automatic feature extraction from raw data in contrast to conventional ANN. Among others, convolutional neural networks (CNN) are one type of most attractive DNN, which replaces general matrix multiplication by convolution operations and thus reduce the network complexity and computation [52]. Usually, deeper neural network would contribute a higher performance, but they are more difficult to train. In this study, in order to further improve the efficiency and accuracy of the non-linear I-V prediction model for PV modules, a relatively new CNN framework named deep residual network (ResNet) [53] is applied to model the PV modules based on raw I-V characteristic data at various operation conditions, which can use residual learning framework to significantly improve the training of CNN.

In addition to selection of ANN or other machine learning algorithms, the performance of the regression based modelling are greatly dependent on the design of model input and output variables and the preparation of the dataset for the training. In view of that DC-AC inverters usually regulate the output voltage to track the maximum power points (MPP), most of the ANN based modeling methods input voltage together with ambient conditions to predict the output current or power. Whereas, some researchers proposed to input current together with ambient conditions for estimating the output voltage or power [39,54]. In terms of the input ambient conditions, many models for common PV modules take into account the measured irradiance and module temperature that are most relevant to the output electrical parameters [39,42,44,47,54,55], which only require common irradiance and temperature sensors in practical applications. However, because concentrator PV (CPV) modules feature a narrow acceptance angle, the angle of irradiance or the direct normal irradiance was required for the modelling [3,40,46,56]. In addition, wind speed was also used for modelling of CPV modules because it has obvious influence on the cell temperature and performance [3,40,56]. But, with the module temperature available, the wind speed is not so correlated to the modeling. Besides, Piliougine et al. proposed to use the solar spectrum as one additional input for improving model accuracy [57], but the spectral information was rarely available. In this study, we focus on the modeling problem of common PV modules, and thus only the irradiance and module temperature will be used. In terms of the electrical input and output, most reported models are single-input single-output (SISO) so as to enable dynamic PV simulation, i.e., they have single voltage input and single current or power output. Usually, SISO models are trained using a set of discrete data points on I-V curves, which cannot utilize the correlation among the data points on an I-V curve to improve the accuracy. In addition, they can be only used to estimate a single data point of I-V curve at a time. Thus, I-V curves or MPP can be identified by dynamic MPPT or traversal of a single model or running several models in parallel, which limits the efficiency. Predication of a whole I-V curve under specific operating condition at a time can obviously improve the efficiency and facilitate the MPPT operation. Therefore, in this study, we propose to build a multi-input multi-output (MIMO) I-V prediction model for PV modules using I-V curves measured at various ambient conditions as the training dataset instead of single data points.

Based on the aforementioned analysis, this study investigates new modeling techniques and mainly makes contributions in the following aspects, so as to improve the modelling of PV modules.

(1) A modified one-dimensional deep residual network (1-D ResNet) is designed and applied for the first time on the black-box modeling problem for PV modules to predict whole I-V characteristics curves at arbitrary operating conditions. The inputs of 1-D ResNet based MIMO PV model are incident irradiance, PV module temperature and predetermined voltage vector of I-V curve, and the outputs are the corresponding current vector. The proposed modeling method is validated using measured I-V curves large datasets of six different types of PV modules provided by National Renewable Energy

Laboratory (NREL) [58].

- (2) A conventional equivalent circuit based white-box PV modelling approach is proposed as well for comparison with the black-box model. The white-box PV modeling consists of two steps of parameter extraction. The first step is to extract the five OPC parameters of single-diode model, and the second step is to extract five STC parameters and two temperature coefficients from the OPC-STC translation equations. The comparison is performed using I-V curves dataset of a PV module. Comparison result validates that the black-box method is obviously better than the white-box based method.
- (3) In view of the fact that operating conditions of measured I-V curves are highly non-uniform, a grid sampling method is applied on the operating conditions (irradiance and temperature) to select part of the I-V curves for training the model, which could alleviate the overfitting issue caused by imbalanced data and help to build a more general model.
- (4) The original NREL datasets contain some abnormal I-V curves that should not be used to train a normal PV model. To address the issue, we propose to use a single-diode model based parameter extraction algorithm to detect the abnormal I-V characteristic curves (such as the ones measured under partial shading conditions) according to the root mean square error (RMSE) of the curve fitting result.
- (5) The proposed ResNet based modeling approach is further compared with some other conventional ANN based black-box modeling methods, including GRNN, ELM and MLP on the six different types of PV modules. Comparison results validate that the proposed DNN method achieves best accuracy and generalization performance on six different PV modules.

The remainder of this article is structured as follows. Section 2 discusses the equivalent circuit based white-box models and corresponding white modeling methods for PV modules. Section 3 details the proposed 1-D ResNet based black-box PV modeling method and the I-V curves dataset provided by the NREL. Experiments, result analysis and methods comparison are carried out in Section 4. Finally, some significant conclusions are drawn.

## 2. Equivalent circuit based white-box modeling of PV modules

The process of conventional white-box modeling are based equivalent circuits and usually consists of four steps: (1) select an appropriate model structure, i.e., equivalent circuits; (2) determine translation relationship of the model parameters with respect to the input irradiance and operating temperature; (3) extract the model parameters under operating conditions (OPC) from measured I-V curves; (4) identify the model parameters under the standard test condition (STC, i.e., the irradiance is  $1000 \text{ W/m}^2$  and the temperature is  $25^\circ\text{C}$ ). In the following, a white-box modeling method is proposed for the commonly used single-diode model, the result of which is compared with the proposed regression based black-box method in Section 4.

### 2.1. Equivalent circuit of the commonly used single-diode white-box PV models

Among all of existing circuit-based models, the single diode model and the double diode model are commonly used. The process for obtaining the model parameters is called parameters extraction problem. The specific equivalent circuit is shown in Fig. 1.

The equivalent circuit equation of the single-diode model for a solar cell is given by Eq. (1). Obviously, there are five unknown parameters ( $I_{pv}$ ,  $n$ ,  $I_o$ ,  $R_s$  and  $R_{sh}$ ) for the single-diode model, which are related to the input irradiance and operating temperature.

$$I = I_{pv} - I_o \left[ \exp\left(\frac{q(V + IR_s)}{nKT}\right) - 1 \right] - \frac{V + IR_s}{R_{sh}} \quad (1)$$

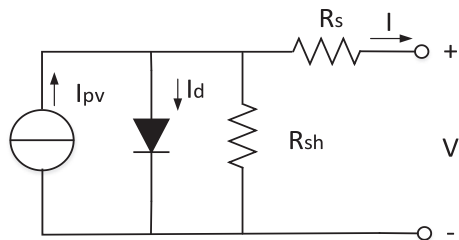


Fig. 1. Equivalent circuit of the single-diode model.

where the  $I_{pv}$  is the photocurrent and  $I_o$  is the saturation current of the diodes; Constant  $q$  is absolute value of electric charge of an electron ( $1.60217646 \times 10^{-19} \text{ C}$ );  $K$  is the Boltzmann constant ( $1.380653 \times 10^{-23} \text{ J/K}$ );  $T$  is the absolute temperature of the PV cell;  $n$  denotes the ideal factor of the diode;  $R_s$  is the equivalent series resistance, and  $R_{sh}$  is the equivalent parallel resistance.

Usually, PV modules/arrays are composed of a certain number of solar cells connected in series and/or in parallel as shown in Fig. 2. In the normal ideal status, the terminal output voltage and current of PV modules/arrays are distributed equally to each solar cell. Hence, the single diode model could be rewritten as follows.

$$I/M_p = I_{pv} - I_o \left[ \exp\left(\frac{q(V/M_S + IR_s/M_p)}{nKT}\right) - 1 \right] - \frac{V/M_S + IR_s/M_p}{R_{sh}} \quad (2)$$

where the  $M_p$  is the number of solar cell strings connected in parallel, while the  $M_s$  represents the number of solar cells in series in a string.

## 2.2. Translation equations of PV model parameters with respect to irradiance and temperature

In addition to the model structure, the translation relationship of model parameters with respect to irradiance and temperature should be then determined for obtaining a complete model. According to the literature [2,30,32], the most commonly adopted translation equations are used and listed in Eqs. (3)–(7).

$$I_{pv} = [I_{pv,STC} + \alpha(T - T_{STC})] \cdot \frac{G}{G_{STC}} \quad (3)$$

$$I_o = I_{o,STC} \left( \frac{T}{T_{STC}} \right)^3 \exp \left[ \frac{1}{K} \left( \frac{E_g}{T_{STC}} - \frac{E_g}{T} \right) \right] \quad (4)$$

$$R_s = R_{s,STC} \cdot \frac{T}{T_{STC}} \cdot \left[ 1 - \beta \cdot \ln \left( \frac{G}{G_{STC}} \right) \right] \quad (5)$$

$$R_{sh} = R_{sh,STC} \cdot \frac{G_{STC}}{G} \quad (6)$$

$$n = n_{STC} \cdot \frac{T}{T_{STC}} \quad (7)$$

where the  $I_{pv,STC}$ ,  $I_{o,STC}$ ,  $R_{s,STC}$ ,  $R_{sh,STC}$  and  $n_{STC}$  are values of the five unknown parameters at the STC condition, while the  $I_{pv}$ ,  $I_o$ ,  $R_s$ ,  $R_{sh}$ ,  $n$  are the corresponding values at operating conditions. The  $\alpha$  represents the temperature coefficient of the photocurrent ( $I_{pv}$ ), which is usually given in the datasheet of PV modules. The  $\beta$  represents the irradiance coefficient of the series resistance ( $R_s$ ). In order to calibrate the actual value, both of  $\alpha$  and  $\beta$  coefficients are regarded as unknown coefficients to be optimized. The  $E_g$  is the energy band gap. The value of  $E_g$  is equal to 1.121 eV for silicon solar cell at STC [32], which is linear with the temperature as given in Eq. (8). The values of the coefficient  $\beta$  was empirically set to 0.217 in [32]. But, to obtain accurate value, it is deemed as an unknown coefficient to be optimized as well.

$$E_g,T = E_{g,STC} \cdot [1 - 0.0002677(T - T_{STC})] \quad (8)$$

## 2.3. Identification of the OPC and STC parameters

Once the model structure and the relationship between the model parameters and operating conditions (irradiance and temperature) are determined, the remaining procedures of measured I-V curves based conventional PV modeling methods are to extract the model parameters at OPC conditions and then identify the STC parameters. Both of the two procedures are based on curve fitting methods, since the relationship equations are fixed and then better fitting usually represents higher accuracy. Curve fitting methods are essentially optimization methods that minimize error objective functions. In this study, a hybrid optimization algorithm (eagle strategy based hybrid adaptive Nelder-Mead simplex, abbreviated EHA-NMS) previously proposed by the authors for the OPC parameter extraction of PV models is used for the curve fitting, which combined artificial bee colony (ABC) meta-heuristic algorithm and Nelder-Mead simplex (NMS) method and features fast convergence, strong robustness and high accuracy. The error objective function is the RMSE as given in Eq. (9). The specific flowchart of the EHA-NMS is shown in Fig. 3(a), which consists of three optimization stages: coarse exploration, coarse exploitation and fine exploitation. In the coarse exploration stage, the ABC algorithms to choose  $N_s$  best food sources with few iterations for avoiding the slow initial convergence of the basic NMS. Then the  $N_s$  best food sources located in first stage will be updated by the NMS algorithm in coarse exploitation stage. In this stage,  $N_s$  best food sources, as  $N_s$  initial points, create new simplexes by running some NMS iterations. Finally, in fine exploitation, the model parameters are further optimized from the best result reserved in the second stages using a new single NMS algorithm with adaptive shrinkage coefficient decreased linearly.

The detailed procedure of the extraction of OPC model parameters from measured I-V curves can be referred to our previous work [59]. In the objective function Eq. (9) for OPC parameters, the  $x_i$  represents the calculated current of the data points on I-V curves by Eqs. (1) and (2), while the  $x_i$  represents the measured current. After obtaining the OPC model parameters from measured I-V curves, the procedure of identification of STC model parameters in the translation equations is illustrated in Fig. 3(b). These unknown parameters include  $I_{pv,STC}$ ,  $I_{o,STC}$ ,  $R_{s,STC}$ ,  $R_{sh,STC}$ ,  $n_{STC}$  and the two coefficients ( $\alpha$  and  $\beta$ ) in the translation equations. In the objective function Eq. (9) for STC parameters, the  $x_i$  is the calculated value of the OPC parameters of each I-V curve, while  $\hat{x}_i$  represents the corresponding extracted OPC parameters. The identification result will be detailed in Section 4.1.

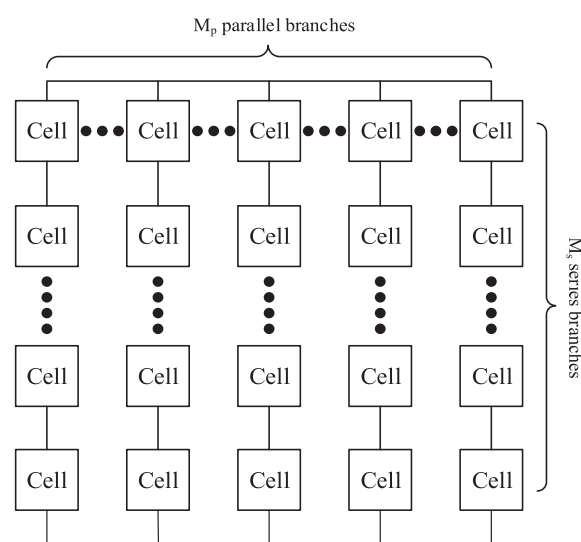
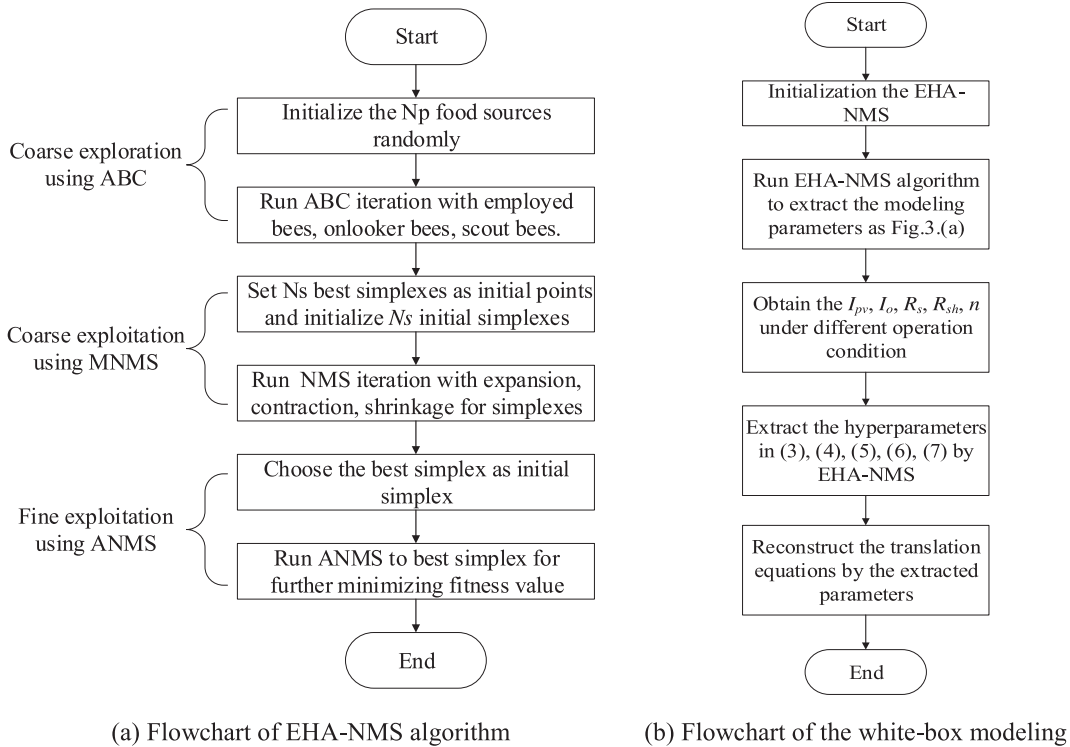


Fig. 2. Illustration of a PV module composed of solar cells.



**Fig. 3.** Flowchart of the EHA-NMS optimization method and the STC parameters extraction.

$$\text{Obj} = \sqrt{\frac{1}{N} \sum_{i=1}^N (\hat{x}_i - x_i)^2} \quad (9)$$

where the  $N$  is the number of the data points in a I-V curve or the number of measured I-V curves.

### 3. Regression based black-box modeling of PV modules using a 1-D ResNet

Different from the equivalent circuit based white-box modeling, regression based black-box modeling is kind of data-driven approaches, which needs no predetermined equivalent circuits and only relies on the measured data to directly build the black-box models. Regression methods can avoid the limitation of the predetermined circuit structures that are hardly accurate for diverse conditions, which are usually based on machine learning algorithms. In view of the highly non-linear behavior and time varying ambient conditions and operating status, we propose to use a relatively new CNN framework 1-D ResNet instead of conventional ANN to perform the regression-based modeling for several types of PV modules using a large number of I-V characteristic curves measured in field. Different from conventional PV modeling methods with single voltage input and single current output, we propose a new model with multiple voltage inputs and multiple current outputs, which can be used to predict the whole I-V curve at a time for a specific operating irradiance and temperature. The I-V curve predication model can significantly improve the model performance and facilitate MPPT process.

In this section, the datasets of experimental I-V curves and corresponding data preprocessing are described firstly. Then, the regression based modeling problem is defined. Lastly, the new 1-D ResNet based modeling approach is detailed.

#### 3.1. Experimental I-V curves and data preprocessing

##### 3.1.1. Original experimental I-V curves dataset

In this study, we use the large measured I-V curves repository

provided by the National Renewable Energy Laboratory (NREL) [58]. In order to validate the feasibility and generalization of the proposed PV modeling method, we selected the I-V curve datasets of six different type of typical PV modules (denoted as A, C, D, E, G and H) measured at the Golden site, whose NREL identifiers are xSi11246, mSi0251, CdTe75669, CIGS1-001, HIT05662 and aSiMicro03038 respectively. Their corresponding solar cell are made of different material and have different electrical characteristics, including single-crystalline silicon, multi-crystalline silicon, cadmium telluride, copper indium gallium, amorphous silicon/crystalline silicon and amorphous silicon/micro-crystalline silicon respectively. In total, their I-V datasets include 71,804 I-V curves, which were measured under various ambient conditions.

The NREL repository not only contain the voltage and current data of I-V curves, but also include the corresponding environment data, including the Plane-of-Array (POA) irradiance, PV module back-surface temperature, meteorological data (such as dry bulb temperature, relative humidity, global horizontal irradiance, diffuse horizontal irradiance, etc.), and so on. In this study, in addition to the I-V curves data, the most relevant POA irradiance and back-surface temperature are used for the modeling. The range of the POA irradiance and temperature for six different modules are limited to be 50–1000 W/m<sup>2</sup> and 0–40 °C, respectively.

##### 3.1.2. Data preprocessing of raw I-V characteristic curves

The repository includes many abnormal I-V curves measured under partial shading conditions, which should be excluded in the PV modeling for a high accuracy. In addition, the distribution of the ambient conditions of the normal I-V curves is highly non-uniform, which will lead to overfitting in the ranges that have more training data and underfitting in the ranges that have less training data. This will greatly affect the generalization performance of the regression. Therefore, one purpose of the data preprocessing is to identify and exclude the abnormal curves. The other purpose of data preprocessing is to resample and obtain I-V curves datasets that have relatively uniform distribution of the ambient conditions for the modeling, which is implemented by a

grid sampling.

(1). *I-V curves down-sampling and abnormal I-V curves detection.* As illustrated in Fig. 4(a) and (b), the I-V characteristic curves measured under normal and partial shading status are depicted. Compared with the normal I-V characteristic curves, the curves measured under the partial shading were obviously distorted and contained multiple power peaks. Usually, the shape of normal I-V curves is similar and is mainly constrained by the underlying physical model equation. Therefore, we use a curve fitting technique to extract the model parameters of commonly used single diode model, and the abnormality of the curve shape can be simply detected by the RMSE of fitting [33]. Specifically, the EHA-NMS optimization algorithm is used again to carry out the curve fitting and thus to exclude the abnormal curves [59]. In the NREL datasets, there are around 175 discrete points for each I-V curve, which greatly increases the computation cost of the I-V prediction. Therefore, before the detection of abnormal I-V curves, all the original I-V curves are down-sampled to be composed of 50 new points. The down-sampling is based on uniform voltage interval and linear interpolation. The voltage range is set to be from 0 to the minimum open circuit voltage  $V_{oc,min}$  in the I-V dataset of the specific modules.

The procedure of I-V curves down-sampling and abnormal I-V curves detection is illustrated in Fig. 5, where  $V_C$  and  $I_C$  is the down-sampling voltage and current of a new data point on a down-sampled I-V curve;  $V_1$  and  $V_2$  are the voltages of the two nearest measured data points around the resampled voltage  $V_C$ ; ResNum is the number of data points of down-sampled I-V curves;  $S_v$  is the down-sampled voltage interval;  $V_S$  and  $I_S$  is the voltage and current vector of the new I-V curve,  $E_C$  is the RMSE fitting error of each I-V curve, and  $E_{th}$  is the RMSE threshold to check if an I-V curve is abnormal. Firstly, the  $V_{oc,min}$  is found from the I-V curve dataset of a specific PV module to determine the down-sampled voltage range; the  $S_v$  is calculated by  $V_{oc,min}/\text{ResNum}$ , and the voltages of down-sampled data points are determined; the  $E_{th}$  is determined empirically. Secondly, the original I-V curve is down-sampled to be a new I-V curve consisting of ResNum data points by an iterative process: the two nearest measured data points of a down-sampled data point are found according the voltage values, and the currents of down-sampled data points are calculated by linear interpolation using the two nearest measured data points and the pre-determined voltage  $V_C$ . And then, the EHA-NMS based curve fitting is performed on the down-sampled I-V curve to obtain the RMSE fitting error  $E_C$ . Finally, the  $E_C$  is compared with the  $E_{th}$  to check if the I-V

curve is abnormal or not. If it is normal, it can be then used for the subsequent PV modeling. Otherwise, it is deleted.

(2). *Grid sampling of the I-V curves.* After excluding the abnormal I-V curves, the distribution of operating conditions of the normal I-V curves for the six types of PV modules is illustrated in Fig. 6, from which it can be observed that the condition distribution is quite non-uniform for all the six types of PV modules. According to the distribution, we found that the majority of the I-V curves remain in the temperature range (0–40 °C) and irradiance range (50–1000 W/m<sup>2</sup>). Therefore, only the I-V curves in the both ranges are used for the modeling. In order to obtain I-V curve datasets with uniform operating conditions for the subsequent regression based modeling, we propose a two dimensional grid sampling method, which is illustrated in Fig. 7 on the PV module xSi11246. In the grids, the intervals of temperature and irradiance are set to be 10 °C and 100 W/m<sup>2</sup> respectively. After separating I-V curves data into the grids, random sampling is applied on every grid for obtaining relatively uniform training datasets. The Matlab pseudo-code of the proposed grid sampling method is shown in Fig. 8. The number of samples  $N_s$  is counted in a particular grid firstly and the threshold values of grid samples  $N_{th}$  are set for different datasets. The sample means an entire I-V curve. The grids with more than  $N_{th}$  samples utilize down-sampling to randomly extract  $N_{th}$  samples as the modeling datasets, in which 70% samples are used as the training dataset and the 30% samples are used as testing dataset. For the grids with less than  $N_{th}$  samples, all the samples are used, and the division of the training and testing datasets are the same as the previous. Finally, during the model training, 10-fold cross validation is used to improve the generalization performance the model. In other words, 90% of the training data is used to train the proposed CNN based model, and 10% of training data is used to validate the model during the training process. In order to trade off both the number of data samples and the uniform distribution, the  $N_{th}$  is set to 300 for datasets of all six different PV modules.

Through the grid sampling, 48,931 I-V characteristic curves are selected for six different PV modules in total. The new distribution of the operating conditions of selected I-V curves by grid sampling is shown in Fig. 9, in which it can be observed that the new distribution is much more uniform than that of the original. However, the samples are not ideally uniform, because the number of samples in some grids is too small.

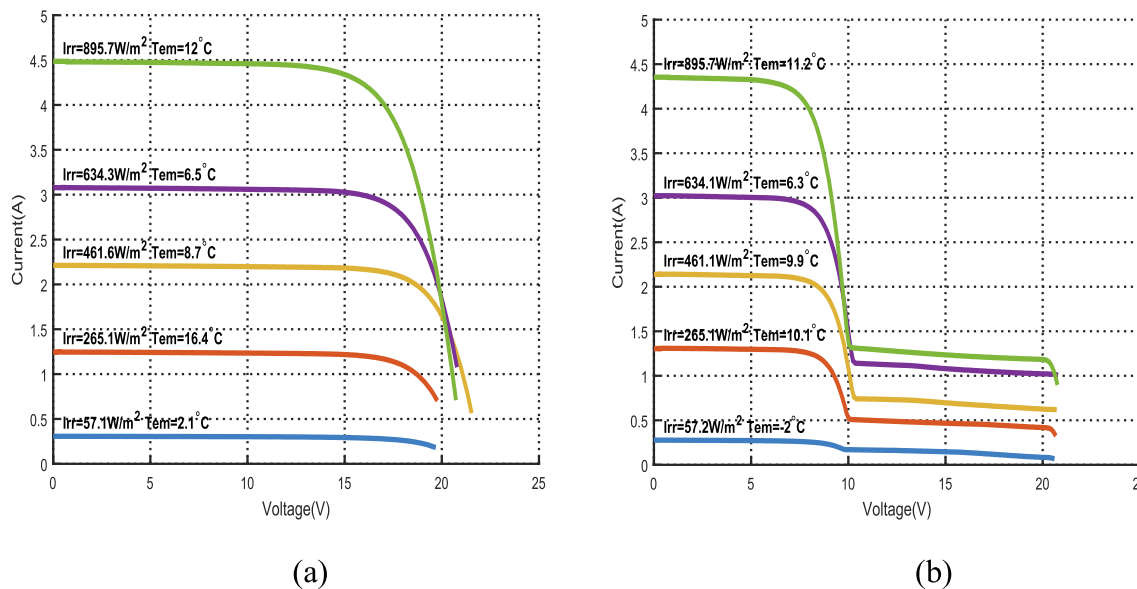
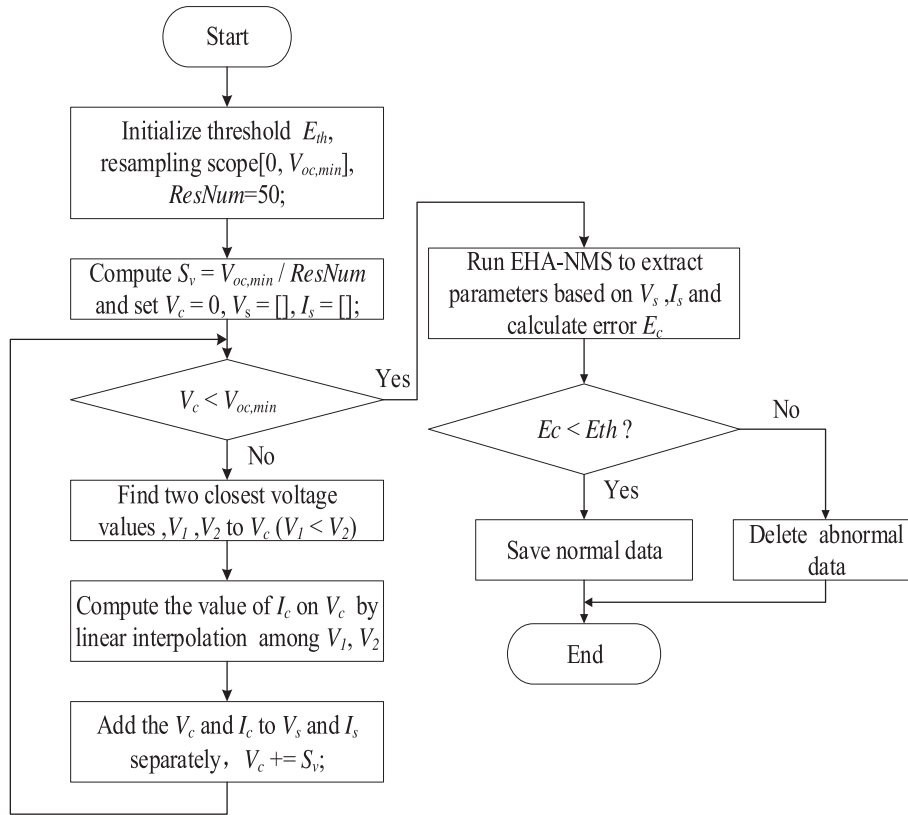


Fig. 4. (a) Normal I-V curves; (b) abnormal I-V curves under partial shading conditions.



**Fig. 5.** Flowchart of data preprocessing for I-V dataset of a PV module.

### 3.2. Regression based PV modeling using 1-D ResNet

As kind of most attractive deep learning techniques, the CNN have emerged as a powerful tool for the feature extraction and non-linear learning, which is widely used in image recognition, object detection, and so on. Compared with fully connected (FC) DNN, there are three major layers in CNN: 1) Convolution layer: acquiring the feature maps from input using a set of kernels with a certain padding to keep the size of the feature maps. 2) Pooling layer: reducing the spatial dimensions of input by the sub-sampling factor called *Stride* in CNN, but not the depth of the feature maps. 3) FC layer: producing the output vector for classification or regression. In aforementioned layers, there are three key hyper-parameters: the kernel size  $k$ , stride  $s$  and padding value  $p$  to determine the size of the extracted feature maps. In Fig. 10, an example of typical two dimensional (2-D) CNN model with an input of RGB three-channel size of  $28 \times 28$  images is illustrated. The pooling layer is added between two adjacent convolution layers to decrease the dimension of the input. The kernel size is set to 5 for the convolution layer and 4 for pooling layer and the number of filters is set to 6 and 12 respectively. In addition, stride is set to 1 and 2 for convolution layer and pooling layer respectively. After obtaining sufficient amount of features by forward propagation, the FC layer is applied to produce the prediction result.

The CNN outperforms conventional ANN in the following three aspects [52]:

- (1) Sparse connection: Unlike the typical layer of neural networks with dense connection, each neuron in adjacent layers is connected to a small part of the corresponding inputs. With the sparse connection, the local connection by setting the kernel smaller than the input can improve the efficiency and decrease the memory.
- (2) Parameters sharing: In a particular feature map, all neurons share with the same parameters of the kernel to compute a convolution of the kernel weights and input. The shared parameters used in the

convolutional layer keep the translation invariance for the CNN architecture. Additionally, it can further reduce the storage requirements.

- (3) Equivalent representation: The output transform is the same as the input transform, which is useful when we pay more attention to the importance of features rather than the specific location.

In summary, as a deep neural network, the CNN are better than conventional ANN, in terms of the non-linear fitting ability, feature representation capability and generalization performance. Due to these merits, in this paper, we investigate and apply 1-D ResNet to model PV modules using large datasets of I-V characteristics curves and their operating conditions.

#### 3.2.1. Problem definition for the 1-D ResNet based PV modeling

In this paper, the output current will be predicted with voltage at the given ambient temperature and solar irradiance. Therefore, the problem of the curve fitting is defined to minimize the following cost /objective function (Mean Square Error) on a part of samples in the datasets called mini-batch in the following:

$$C = \frac{1}{MN} \sum_{j=1}^M \sum_{i=1}^N (\hat{I}_{i,j} - I_{i,j})^2 \quad (10)$$

where  $\hat{I}$  is the predicted current and  $I$  is the measured current. The  $N$  is number of the total number of available points in an I-V characteristic curve and  $M$  is the number of the mini-batch size.

#### 3.2.2. Architecture of the proposed 1-D ResNet

Inspired by the 2-D CNN plain network architecture, we propose to predict the output I-V characteristic curves of PV modules at arbitrary ambient conditions using a 1-D ResNet that is composed of a convolutional layer with pooling layer as input, five residual blocks and a fully connected layer as regression, as shown in Fig. 11 (where the conv

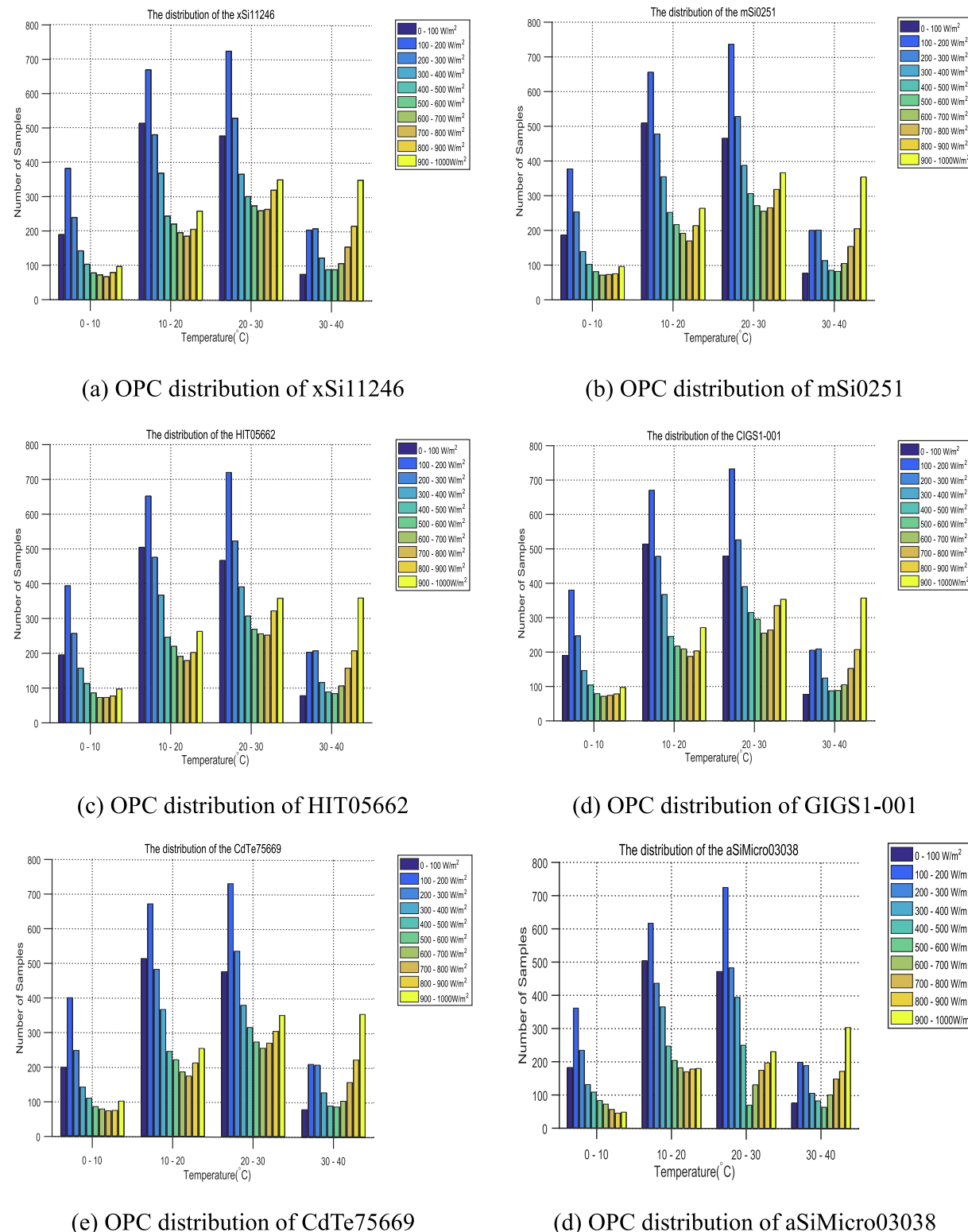


Fig. 6. Distribution of the operating conditions of the original datasets for six different PV modules.

is the 1-D convolution layer. In the *conv*, the first parameter is the value of kernel size, followed by the value of the output channels and finally optional parameter is value of stride). Residual block refers to two convolutional layers with a shortcut connection [60–62]. The input of the 1-D ResNet model includes solar irradiance, ambient temperature and voltage vector, while the output is the corresponding current vector. The specific configuration of the proposed 1-D ResNet model is

detailed in Table 1. In order to match the dimension, the value of the kernel size  $k$  for first pooling layer and convolution layer in Residual Block\_4 is set to 4 and the rest of the modules are set to 3 as [62] and the stride are usually set to 1 or 2 respectively. The padding value of all the middle layers is set to 1 to ensure that the dimensions inside the residual block are same.

Compared with 2-D CNN plain network structures in Fig. 10, the

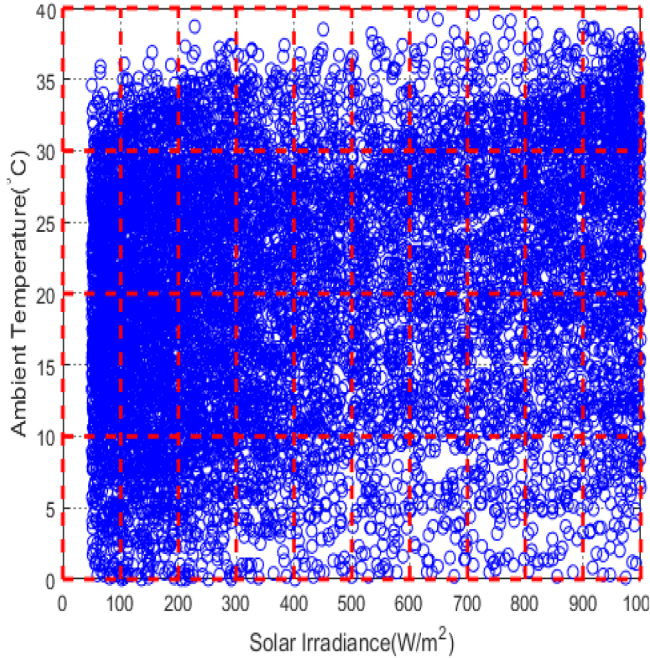


Fig. 7. Illustration of the grid sampling.

#### %% Initialization:

```
Set baseTemp = 0, baseIrr = 0, MaxTemp = 40, MaxIrr = 1000,
IrrInterval=100, TempInterval=10, Nth=300;
```

Load datasets

#### %% Grid Sampling

```
for baseTemp:TempInterval:MaxTemp
    for baseIrr:IrrInterval:MaxIrr
        % Select the samples in one groups
        Calculate the number of the samples Ns;
        Shuffle the samples in one group;
        if Ns<= Nth*70%
            Randomly select 70% samples as training samples;
            Save 90% percent of training samples as training set;
            Save 10% percent of training samples as cross validation set;
            Randomly select another 30% samples as test samples;
```

else

```
    Randomly select Nth*70% samples as trained samples;
    Save 90% percent of training samples as training set;
    Save 10% percent of training samples as cross validation set;
    Randomly select Nth*30% remained samples as test samples;
```

end

Save the training samples and test samples;

end

#### %% Save dataset

```
Save training set;
Save cross validation set;
Save test set;
```

end

Fig. 8. The pseudo-code for gird sampling.

primary structural difference for the proposed 1-D ResNet is to replace the 2-D matrices with 1-D arrays for both kernels and feature maps. Accordingly, the 2-D matrix computation is replaced by its 1-D counterpart. When the size of the input is ( $C_{in}, L$ ) and output dimension is ( $C_{out}, L_{out}$ ), the value of output can be described as Eq. (11) by 1-D convolution manipulation. In addition, the output for FC is given by Eq. (12) and the non-linear activation functions, like ReLU defined in Eq. (13), are added between adjacent layers to increase the nonlinearity as Eq. (14).

$$z^{(l)} = b^{(l)} + \sum_{k=0}^{C_{in}-1} w_{C_{in}j,k} * a^{(l-1)} \quad (11)$$

$$z^{(l)} = w^{(l)} a^{(l-1)} + b^{(l)} \quad (12)$$

$$\text{ReLU}(x) = \begin{cases} 0, & x < 0 \\ x, & x \geq 0 \end{cases} \quad (13)$$

$$a^{(l)} = g(z^{(l)}) \quad (14)$$

where  $b^{(l)}$  is the bias in the  $l$ -layer,  $w_{C_{in}j,k}$  is the kernel size from  $k^{th}$  input neuron to  $j^{th}$  output neuron in  $l$ -layer. The  $C_{in}$  and  $C_{out}$  are the numbers of the channels for input layer and output layer respectively. The  $*$  is the 1-D convolution manipulation without zero padding. The  $z^l$  is the activations of the  $l$ -layer and the  $a^l$  represents the activation value for each neurons calculated by nonlinear activation function  $g(\cdot)$ .

In order to further improve the performance of the 1-D CNN and the training speed, the batch normalization [63] and residual block [62] are added to avoid the problems of vanishing/exploding gradient in the deep CNN. Firstly, the Batch Normalization (BN) is a technique to make the layer of the neural network meet normal distribution. In addition, it is utilized to normalize the input parameters and overcome the covariate shift existed in the training process by scaling the previous activations, which improve the sensitivity of the activation function. Therefore, in this paper, BN is inserted into each linear layer and activation function to improve the stability of the neural network. In terms of the application, in this paper, BN normalizes the values of previous activations  $z^l$  by Eqs. (15)–(17) [63]. After adding BN, the forward propagation formula Eq. (14) is changed to be Eq. (18) accordingly.

$$\mu_{\beta} = \frac{1}{M} \sum_{i=1}^M x_i \quad (15)$$

$$\sigma_{\beta}^2 = \frac{1}{M} \sum_{i=1}^M (x_i - \mu_{\beta})^2 \quad (16)$$

$$y_i = \gamma \frac{x_i - \mu_{\beta}}{\sqrt{\sigma_{\beta}^2 + \epsilon}} + \beta \quad (17)$$

$$a^{(l)} = g(BN(z^{(l)})) \quad (18)$$

where the  $M$  is the number of the mini-batch size and  $x$  is the inputs of the BN. The  $\mu_{\beta}$  and  $\sigma_{\beta}$  are the mean and variance for the mini-batch outputs. The output  $y$  of BN has parameters  $\gamma$  and  $\beta$ , which are learned during the training process. The constant  $\epsilon$  is a small number set to be 0.00001 by default.

In addition, the residual block is employed, which adds shortcut connections into plain networks [62]. Compared with the plain full-connected block in Figs. 12(a) and 10, the residual block is built by attaching a shortcut connection as Fig. 12(b). Thanks to the special connection strategy, it makes feature information easier to flow between layers, which can alleviate the overfitting and gradient vanishing. Correspondingly, the process of the forward propagation with residual blocks is changed to be Eqs. (19) and (20) from Eq. (18) for the proposed 1-D ResNet, of which the forward pass directly by Eq. (19) when the dimensions of input and output are same (solid line in the Fig. 11). Otherwise, the channel is recalibrated by another convolution layer as Eq. (20) (dashed line in Fig. 11).

$$y = \text{ReLU}(BN(z^{(l)}) + x) \quad (19)$$

$$y = \text{ReLU}(BN(z^{(l)}) + W_s x) \quad (20)$$

where the  $x$  and  $y$  are the inputs and outputs of the residual block. The  $W_s$  is a matrix to match the dimension of the  $x$  and  $y$ .

In summary, the 1-D ResNet with one input layer, five residual blocks and fully connected layer is designed in this paper. There are three advantages in the proposed structure of the ResNet as follows: (1)

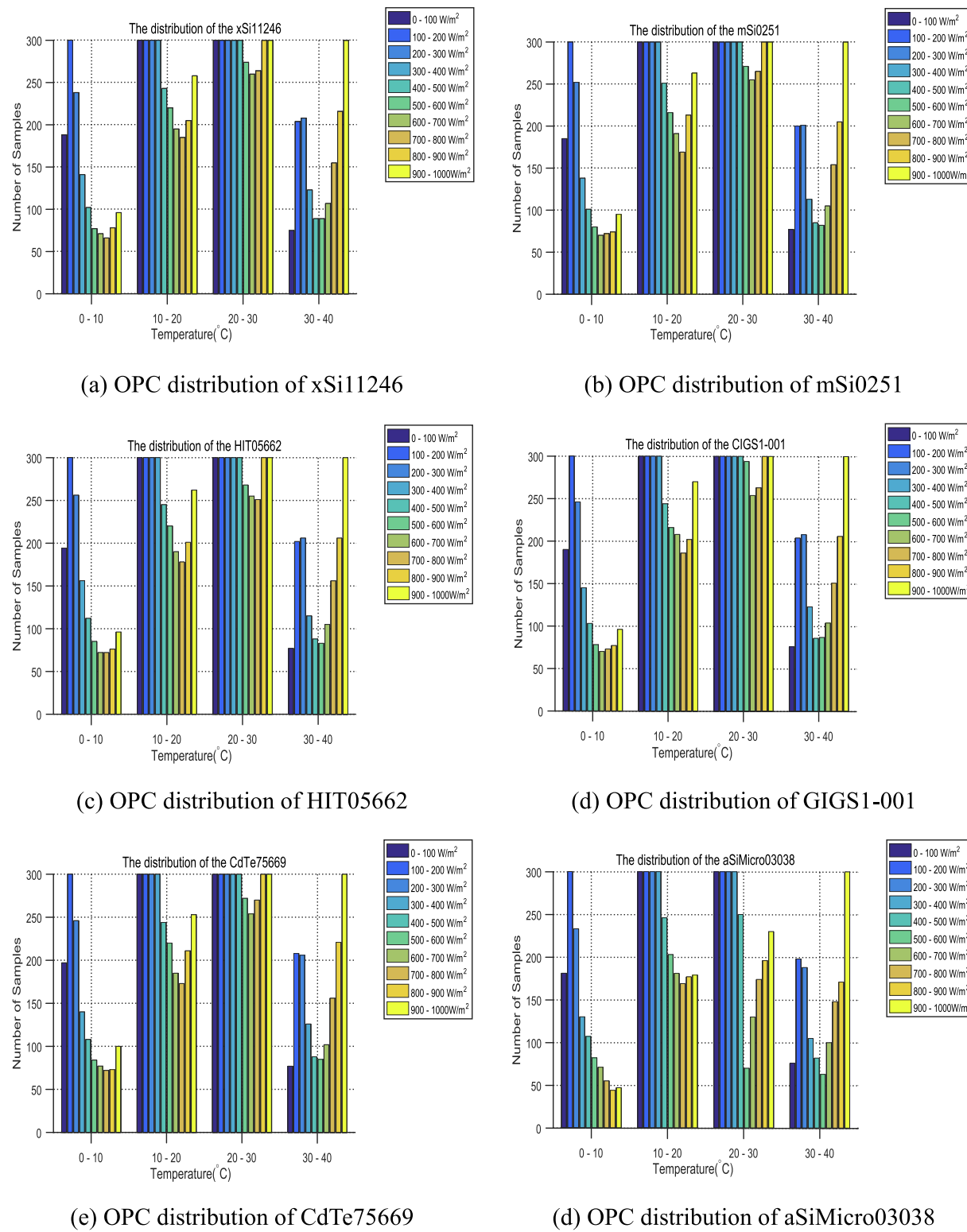


Fig. 9. Distribution of the operating conditions of new datasets of six different PV modules.

The proposed 1-D ResNet can automatically extract the more complex features based on data without subjective factors influenced by different experiences coming from different expert. (2) More related features between adjacent features are learned by the proposed 1-D ResNet through convolution computation. (3) The residual block can improve the performance of the network and avoid the vanishing gradient effectively during end-to-end training. (4) The combination of CNN layer and residual block can greatly promote the computation efficiency and

decrease the memory storage. Although the structure of the 1-D ResNet is flexible and configurable and the performance of the proposed 1-D ResNet may be further improved when more residual blocks are added in theory [62,64], we try to design a ResNet structure with good tradeoff between accuracy and efficiency in this study. The proposed structure with five residual blocks is empirically found achieve optimal tradeoff for the PV modeling problem, since deeper ResNet do not contribute obviously higher accuracy but need obviously higher

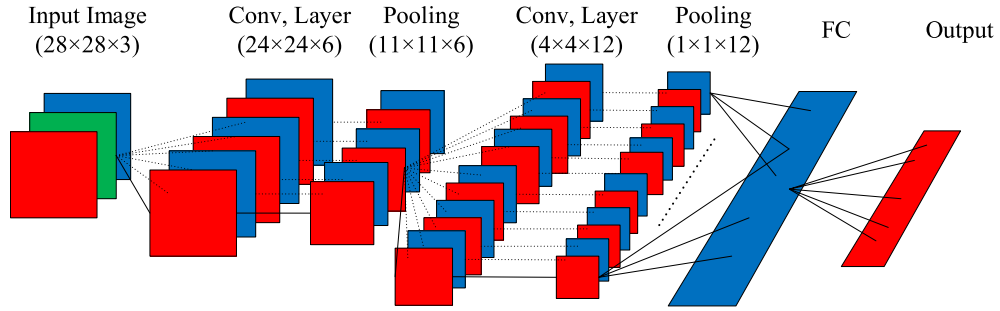


Fig. 10. Overview of a typical 2-D CNN plain network.

computation complexity.

### 3.2.3. Training of the 1-D ResNet based PV model

In order to obtain the predictive model, the proposed 1-D ResNet is trained utilizing the training data with backpropagation (BP) algorithm. The BP was firstly proposed in [65], which has become a major mean for updating parameters during training process. Although it is based on accurate mathematical reasoning and has wide application, every iteration of the parameters requires iterative computation for all training samples that could result in a large consumption of computing

resources and slow convergence. In addition, the learning rate is set to a constant, whose value is too large to cause shocks and even no convergence, but too small to bring out slow convergence. Many other optimization algorithms were proposed to overcome the drawbacks of the basic gradient descent. For example, stochastic gradient descent (SGD) and mini-batch SGD were proposed to update the internal parameters in each iteration with a part of training set, both of which can decrease the computational cost and promote the convergence speed. The pseudo-code of the mini-batch gradient descend with backpropagation is shown in Fig. 13.

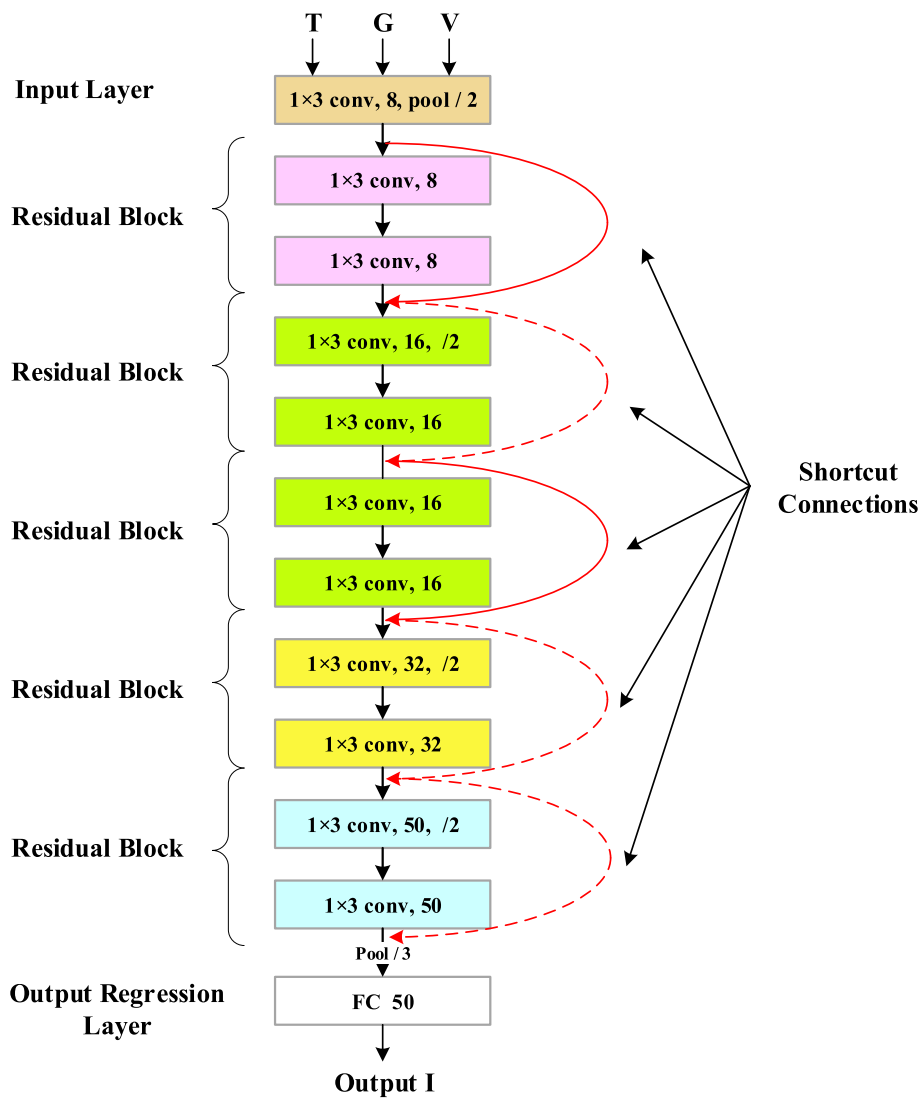


Fig. 11. Architecture of the proposed 1-D ResNet based PV model.

**Table 1**  
Detailed configuration of the proposed 1-D ResNet.

Layer name	Output dimension	Detailed architecture for the proposed ResNet
Input Layer	$1 \times 52, 8$	$k = 1 \times 3, 8, ss = 1, p = 1$
Residual Block_1	$1 \times 25, 8$	$k = 1 \times 4, \text{maxpooling}, ss = 2, p = 1$ $\begin{bmatrix} k = 1 \times 3, 8, ss = 1, p = 1 \\ k = 1 \times 3, 8, ss = 1, p = 1 \end{bmatrix}$
Residual Block_2	$1 \times 12, 16$	$\begin{bmatrix} k = 1 \times 3, 16, ss = 2, p = 0 \\ k = 1 \times 3, 16, ss = 1, p = 1 \end{bmatrix}$
Residual Block_3	$1 \times 12, 16$	$\begin{bmatrix} k = 1 \times 3, 16, ss = 1, p = 1 \\ k = 1 \times 3, 16, ss = 1, p = 1 \end{bmatrix}$
Residual Block_4	$1 \times 5, 32$	$\begin{bmatrix} k = 1 \times 4, 32, ss = 2, p = 0 \\ k = 1 \times 3, 32, ss = 1, p = 1 \end{bmatrix}$
Residual Block_5	$1 \times 3, 50$	$\begin{bmatrix} k = 1 \times 3, 50, ss = 1, p = 0 \\ k = 1 \times 3, 50, ss = 1, p = 1 \end{bmatrix}$
Output Layer	$1 \times 50, 1$	$k = 1 \times 3, \text{maxpooling}, ss = 1, p = 0$ 50-d FC output

In Fig. 13, the gradient is calculated by the backpropagation error  $\delta^l$  that is deduced from deviation from output layer and the conv1D is the regular 1-D convolution. In the updating process, the  $\nabla_a C$  is the derivative of cost function and  $\odot$  represent Hadamard product. The  $lr$  and  $m$  are the learning rate and mini-batch size. The up( $\cdot$ ) is a function for upsampling and the rev( $\cdot$ ) reverses the 1-D input vector.

The SGD with momentum method [66], which changes weights change in terms of the previous weight change and current gradient, is able to accelerate the directions of low-curvature. The Adagrad [67] is an adaptive gradient algorithm, which works well in sparse gradients. However, the learning rate keeps to decrease and eventually can be closer to 0, at which point the parameters are no longer to update. The RMSProp [68] solves the problem of diminishing learning rates rapidly for Adagrad by a moving average of squared gradient and slows down the shocks when the parameters descent. Ref. [69] proposed another adaptive learning rate adjustment algorithm, i.e., adaptive moment estimation (Adam) that combined the advantages of AdaGrad and RMSProp and achieved stronger robustness and better performance for non-convex optimization. Therefore, in this paper, the Adam, whose process is shown in Fig. 14, is chosen to train the proposed 1-D ResNet from scratch using Python script.

In Fig. 14, the  $\beta_1, \beta_2$  are the decay rates for first and second moment estimate.  $\varepsilon$  is a small constant (i.e.  $\varepsilon = 1e - 8$ ) for stability of algorithm.  $\theta$  is the parameter vector that needs to be optimized (i.e. the weights and bias in the training process).  $s$  and  $r$  represent first and second raw moment estimate respectively. The  $iter$  and  $MaxIter$  are the number of current iteration and stopping criteria. The  $grad$  is the gradient of the for the cost function  $C$  at  $iter$ , which is obtained from backpropagation and  $f(\cdot)$  is used to express the mapping relationship between the inputs and outputs.

Corresponding hyperparameters and parameters are initialized as follows: the proposed 1-D ResNet are trained by Adam with 4096 mini-batch size. The initial learning rate  $lr$  is set to 0.001, and  $\beta_1$  and  $\beta_2$  are initialized as 0.95 and 0.99 respectively. In addition, the learning rate is multiplied by the decay factor 0.45 in every 2000 iterations to provide the smaller initial learning rate. Here, maximum iteration Epoch is set to 50,000 for each model. The appropriate initial parameters can greatly improve the convergence speed and final result. The Xavier as an initialization method is utilized to set initial weights between adjacent layer with same variance for higher convergence speed and better quality of the model, which is detailed in original paper [70]. The dropout [71] are not utilized in this ResNet model to deal with the overfitting. Finally, the proposed ResNet, of which the weights, bias and hyperparameters are initialized as the aforementioned, is properly trained using training dataset. The specific flowchart for the training process of the proposed algorithms is depicted in Fig. 15. In each epoch, the prediction is obtained by forward propagation with the weights and bias acquired from last epoch or initialization. The generalization model is reserved when the updated network has better performance than the best model recorded in the previous epoch on the cross validation set. Then, the weights and bias are updated by Adam optimization based on the gradient back-propagated until the epoch exceeds the maximum iteration. The trained ResNet reserved in the end is considered to be the model with the best generalization for the specific PV modules. In the next section, the comparison result is given based on the benchmark dataset for six different PV modules.

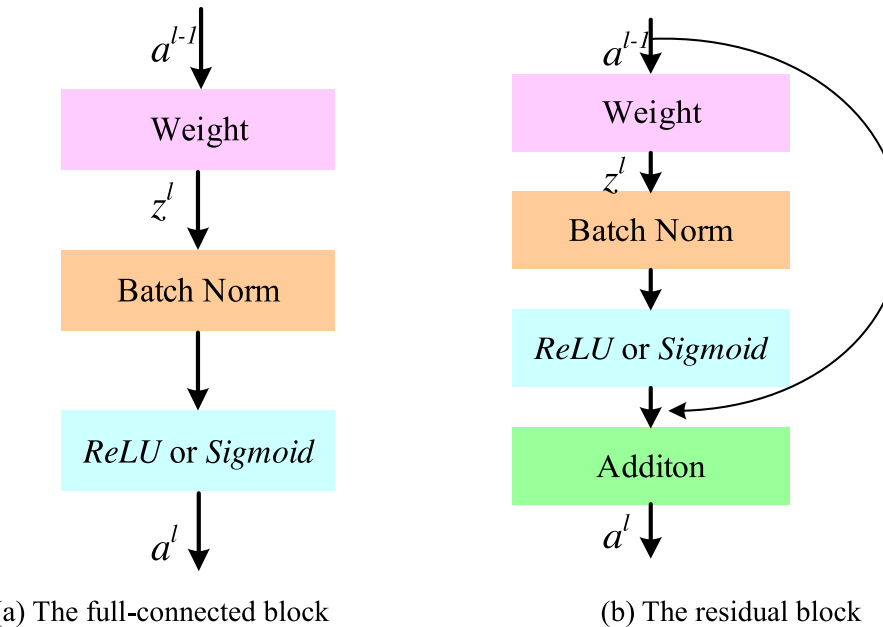


Fig. 12. Different blocks for the proposed CNN.

**Step 1.** Initialize the weight  $w$  and bias  $b$  randomly;

**Step 2.** Set activation value in input layer:  $a^1 = x$ ;

**Step 3.** Perform forward propagation by Eqs. (11), (12), (14), (19) and (20);

**Step 4.** Compute the gradient  $\frac{\partial C}{\partial w}$  and  $\frac{\partial C}{\partial b}$  for FC layer as follows:

**Step 4.1.** Deduce  $\frac{\partial C}{\partial w} = \frac{\partial C}{\partial a^l} \cdot \frac{\partial a^l}{\partial z^l} \cdot \frac{\partial z^l}{\partial w^{l-1}} = \frac{\partial C}{\partial z^l} \cdot a^{(l-1)}$ ,  $\frac{\partial C}{\partial b^l} = \frac{\partial C}{\partial a^l} \cdot \frac{\partial a^l}{\partial z^l} \cdot \frac{\partial z^l}{\partial b^l} = \frac{\partial C}{\partial z^l}$ ;

**Step 4.2.** Compute the deviation  $\frac{\partial C}{\partial z^L}$  in the output layer using  $\delta^L = \frac{\partial C}{\partial z^L} = \nabla_a C \odot g'(z^{(L)})$ ;

**Step 4.3.** Compute the back-propagation error by  $\delta^l = ((w^{l+1})^T \delta^{l+1}) g'(z^{(l)})$  for FC layer,  $\delta_k^{l-1} = up(\delta_k^l) \odot g'(z^{(l-1)})$  for pooling layer,  $\delta_k^{l-1} = \delta_k^l * rev(w^l) \odot g'(z^{(l-1)})$  for 1-D convolution layer;

**Step 4.4.** Compute the  $\frac{\partial C}{\partial w}$  and  $\frac{\partial C}{\partial b}$  by  $\frac{\partial C}{\partial w^l} = a^{(l-1)} \odot \delta^l$ ,  $\frac{\partial C}{\partial b^l} = \delta^l$ ;

**Step 5.** Update the weights and bias as follows:  $w^l = w^l - \frac{lr}{m} \sum_{i=1}^m \frac{\partial C_i}{\partial w^l}$ ,  $b^l = b^l - \frac{lr}{m} \sum_{i=1}^m \frac{\partial C_i}{\partial b^l}$ .

**Fig. 13.** Pseudo-code of mini-batch SGD algorithm for 1-D CNN and FC layer.

**Step 1.** Initialize hyperparameters  $lr$ ,  $\beta_1$ ,  $\beta_2$ ,  $\varepsilon$ ,  $MaxIter$ ;

**Step 2.** Initialize the parameters  $\theta$  and set  $s = 0$ ,  $r = 0$ ,  $iter$ ;

**Step 3.** Update the parameters when  $iter < MaxIter$ :

**Step 3.1.** Increase counters  $iter = iter + 1$ ;

**Step 3.2.** Compute  $grad = \frac{1}{m} \nabla_\theta \sum_{i=1}^m C(f(x^{(i)}; \theta), y^{(i)})$ ;

**Step 3.2.** Compute  $s_{iter} = \beta_1 \cdot s_{iter-1} + (1 - \beta_1) \cdot grad_{iter}$ ;

**Step 3.3.** Compute  $r_{iter} = \beta_2 \cdot r_{iter-1} + (1 - \beta_2) \cdot grad_{iter}^2$ ;

**Step 3.4.** Compute  $\hat{s} = \frac{s}{1 - \beta_1 \cdot iter}$  and  $\hat{r} = \frac{r}{1 - \beta_2 \cdot iter}$ ;

**Step 3.5.** Update parameters  $\theta$ :  $\theta = \theta - lr \frac{\hat{s}}{\sqrt{\hat{r} + \varepsilon}}$ ;

**Step 4.** Return the optimal solution  $\theta$ ;

**Fig. 14.** Pseudo-code of the Adam optimization algorithm.

#### 4. Experiments and result analysis

##### 4.1. Results of the equivalent circuit based white-box PV modeling

In this section, we verify the performance of the single-diode model detailed in Section 2, using the experimental I-V curve dataset of single-crystalline silicon PV module with NREL identifier xSi11246. From the original I-V curve dataset, 5237 training samples and 2493 test samples are obtained by the grid sampling. The training samples are used to build the single-diode model, while the test samples are used to test the performance of the model. As discussed in sub-Section 2.2, the EHA-NMS optimization algorithm is firstly used to extract the five OPC parameters for each training curve. Based on the extracted OPC parameters dataset together with corresponding temperature and irradiance, the EHA-NMS is then applied again to extract the five STC parameters and the other two coefficients  $\alpha$  and  $\beta$  in the Eqs. (3)–(7). The lower bound and upper bound of parameters to be extracted and the hyperparameters of the EHA-NMS algorithm for two sub-problems are given in Tables 2–4, where the MaxObjCal, Np, Limit,  $\rho$ ,  $\chi$ ,  $\gamma$  and  $\sigma$  are the controlling parameters for EHA-NMS detailed in [59]. The values of the final extracted seven parameters are given in Table 5.

After extracting the final seven parameters of the translation equations for the xSi11246 PV module, the irradiance and temperature of each test I-V curve are input into translation equations Eqs. (3)–(7) to

calculate the corresponding five OPC parameters of the single-diode model and thus to obtain the corresponding simulated I-V curves. The distribution of the calculated OPC parameters (marked by red circles) and extracted OPC parameters (marked by blue circles) with respect to the irradiance and temperature are shown in Fig. 16, from which it can be observed that the parameters  $I_o$  and  $n$  have a large deviation. According to Fig. 16(a), the parameter  $I_o$  obviously varies with the irradiance. But, it is only considered to be related to the temperature as shown in the Eq. (4), which may lead to a big error. In terms of ideal factors  $n$ , the linear relationship provided by Eq. (7) also causes a large error between the actual parameters and predictions, which would greatly affect the model accuracy as well. From Fig. 16(c)–(e), we can see that the simulated parameters  $R_s$ ,  $R_{sh}$ ,  $I_{ph}$  are relatively close to the extracted parameters. Therefore, assume that the extracted parameters are the ground true values, the accuracy of the equivalent circuit based model are greatly affected by the selection of the translation relationship between the OPC parameters and the irradiance and temperature.

To illustrate the performance of the equivalent circuit based white-box model, five I-V curves measured under different operation conditions selected from test set are compared with their simulated ones, as shown in Fig. 16(f). It can be observed that there is obvious deviation between the measured and simulated curves, and the magnitude of deviation is related to the operating condition. We further verify the proposed white-box model on the aforementioned test samples, and the statistical result of the RMSE values is given in Table 7 so as to compare with other black-box models.

##### 4.2. Result of the regression based black-box PV modeling

In this section, the proposed 1-D ResNet CNN is comprehensively tested on the experimental datasets of six different types of PV modules (NREL identifier: xSi11246, mSi0251, CdTe75669, CIGS1-001, HIT05662 and aSiMicro03038) that totally contain 48,931 I-V characteristics curves extracted by the grid sampling, as detailed in sub-Section 3.1. For evaluating the superiority of the proposed algorithm, three conventional ANNs are used for comparison in terms of the accuracy and generalization, including the GRNN, ELM and MLP. The ELM consists of 500 hidden neurons, while MLP with single-hidden layer whose number of hidden neurons is 355 suggested in [41]. The GRNN shows good performance for regression problem with four fully-connected layers. The hyperparameter *spread* of the GRNN is automatically chosen by SCE [72] with least RMSE for cross validation during the training process. The specific setting for three conventional

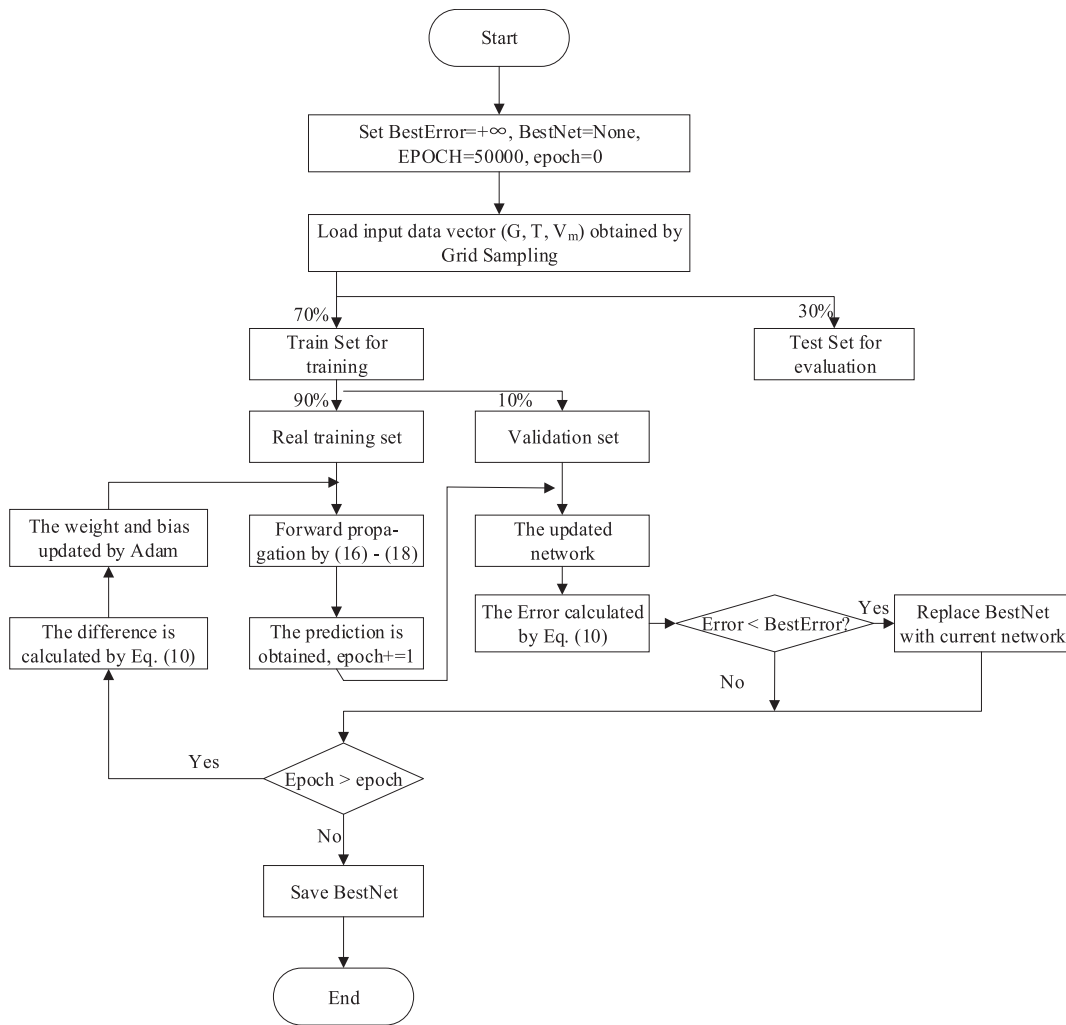


Fig. 15. Training process of the proposed 1-D ResNet.

**Table 2**  
Parameters range of the PV modeling for xSi11246.

Parameters	Lower bound	Upper bound
$I_{pv}$ (A)	0	10
$I_o$ ( $\mu$ A)	0	100
$R_s$ ( $\Omega$ )	0	50
$R_{sh}$ ( $\Omega$ )	0	5000
$n$	1	100

**Table 3**  
Parameters of the EHA-NMS.

Properties	Parameters values
Initialization	Parameter Extraction: MaxObjCal = 5000 Translation Equations: MaxObjCal = 3000
ABC Coarse Exploration	MaxIter = MaxObjCal/2; Number of Food Sources: Np = 20
Multiple NMS Coarse Exploitation	Limit: dim * Np; Number of simplex: Ns = 10 $\rho = 1, \chi = 1 + 2/\text{dim}, \gamma = 0.75\text{-dim}/2,$ $\sigma = 1-1/\text{dim};$
Adaptive NMS fine Exploitation	$\rho = 1, \chi = 1 + 2/\text{dim}, \gamma = 0.75\text{-dim}/2,$ $\sigma_{\min} = 0.005$ $\sigma_{\max} = 1-1/\text{dim};$

**Table 4**  
Parameters range of the translation equations for xSi11246.

Translation equations	Parameters	Lower Bound	Upper Bound
(3)	$I_{pv,STC}$ (A)	0	10
	$\alpha$	0	0.1
(4)	$I_{o,STC}$ ( $\mu$ A)	0	100
(5)	$R_{s,STC}$ ( $\Omega$ )	0	10
(6)	$\beta$	-1	1
(7)	$R_{sh,STC}$ ( $\Omega$ )	0	3000
	$n_{STC}$	0	100

**Table 5**  
Final extracted parameters.

Translation equations	Parameters	Extracted Values
(3)	$I_{pv,STC}$ (A)	4.94045
	$\alpha$	0.00398
(4)	$I_{o,STC}$ ( $\mu$ A)	3.67016
(5)	$R_{s,STC}$ ( $\Omega$ )	0.26527
(6)	$\beta$	-0.39715
(7)	$R_{sh,STC}$ ( $\Omega$ )	132.297
	$n_{STC}$	52.7800

ANN is listed in Table 6. In addition, the proposed 1-D RestNet CNN and the MLP are implemented by Pytorch and trained by Pycharm, while the ELM and GRNN are tested in Matlab R2016a. All the algorithms are

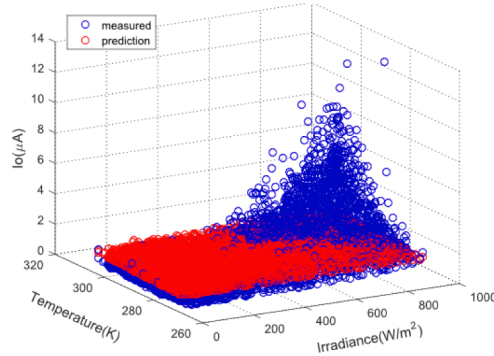
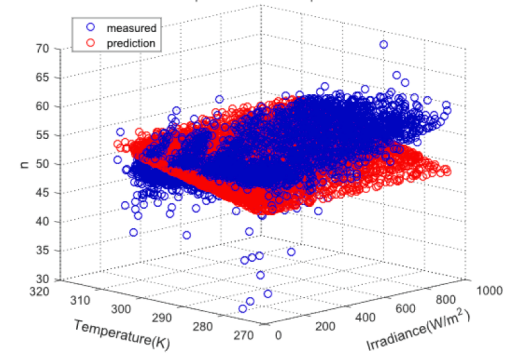
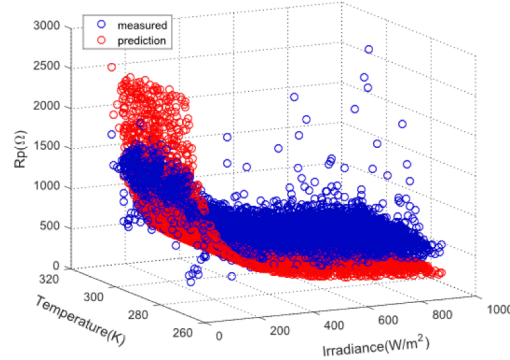
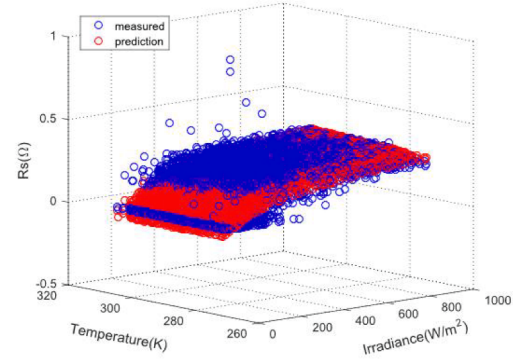
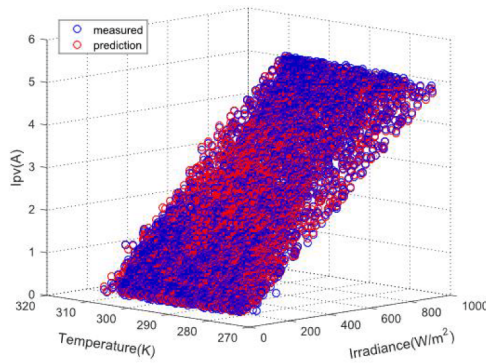
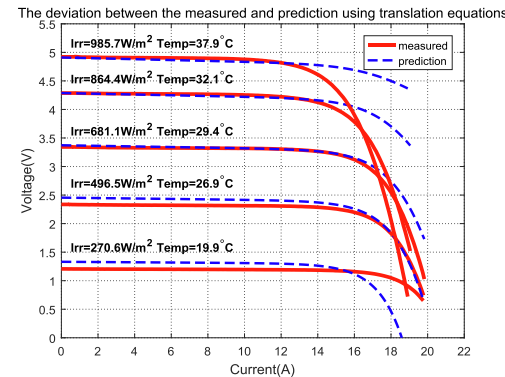
(a) Correlation between  $I_o$  and operating conditions(b) Correlation between  $n$  and operating conditions(c) Correlation between  $R_{sh}$  and operating conditions(d) Correlation between  $R_s$  and operating conditions(e) Correlation between  $I_{pv}$  and operation conditions

Fig. 16. Validation result for the translation equations and white-box model.

**Table 6**  
Setting of hyperparameters for the three conventional ANN based model.

	GRNN	ELM	MLP			
	Spread	Neurons	Neurons	$A$	$\beta_1$	$\beta_2$
xSi11246	0.207553	500	355	0.001	0.95	0.99
mSi0251	0.177697	500	355	0.001	0.95	0.99
CdTe76559	0.184296	500	355	0.001	0.95	0.99
CIGS1-001	0.176532	500	355	0.001	0.95	0.99
HIT05662	0.283995	500	355	0.001	0.95	0.99
aSiMicro03038	0.208861	500	355	0.001	0.95	0.99

run at a desktop computer with the configuration: Intel (R) Core (TM) i5-4430S CPU @ 2.7 GHz, 16 GB (RAM), 2G GTX750Ti (GPU), and 64bits Window 10 operation system.

$$RMSE = \sqrt{\frac{1}{N} \sum_{i=1}^N (\hat{I}_i - I_i)^2} \quad (21)$$

$$nRMSE = \frac{RMSE}{I_{max} - I_{min}} \quad (22)$$

The RMSE and normalized RMSE (nRMSE) defined by Eqs. (21) and (22) are used as the metrics to quantify the prediction error of each I-V curve. In contrast to the RMSE, the nRMSE facilitates the comparison

**Table 7**

Comparison of the black-box models on xSi11246.

Algorithm	Process	Amount	RMSE		nRMSE	
			Mean	Std	Mean	Std
White Box	Training set	5237	7.278E−01	4.855E−01	5.801E−01	2.158E−01
	Test set	2493	7.293E−01	4.799E−01	5.140E−01	4.799E−01
ELM	Training set	5237	4.515E−02	3.401E−01	6.142E−02	9.795E−02
	Validation set	597	5.014E−02	5.164E−02	7.600E−02	3.417E−01
	Test set	2493	4.600E−02	4.115E−02	6.676E−02	1.559E−01
MLP	Training set	5237	2.174E−02	1.913E−02	1.901E−02	1.861E−02
	Validation set	597	2.422E−02	2.457E−02	2.015E−02	1.884E−02
	Test set	2493	2.130E−02	1.916E−02	1.901E−02	1.912E−02
GRNN	Training set	5237	2.772E−02	1.994E−02	3.829E−02	5.565E−02
	Validation set	597	8.436E−02	1.167E−01	8.598E−02	1.182E−01
	Test set	2493	7.806E−02	7.886E−02	8.699E−02	1.435E−01
1-D ResNet	Training set	5237	<b>6.846E−03</b>	<b>4.533E−03</b>	<b>7.829E−03</b>	<b>9.473E−03</b>
	Validation set	597	<b>8.967E−03</b>	<b>1.317E−02</b>	<b>8.676E−03</b>	<b>9.391E−03</b>
	Test set	2493	<b>8.130E−03</b>	<b>1.042E−02</b>	<b>8.647E−03</b>	<b>9.833E−03</b>

between the I-V characteristic curves under different operating conditions. To objectively compare the performance of different models, statistical analysis is performed on the RMSE and nRMSE of I-V curves in the training, validation and test datasets respectively. The mean value of the RMSE and nRMSE can represent the average training/validation/testing accuracy of the models, while the standard deviation of the metrics is used to evaluate the stability of the models under different ambient conditions. The comparison result for six different PV modules are given in Tables 7–12 respectively, where the *Amount* in the tables represents the number of curves of the corresponding dataset and the values in bold are the best. The *Mean* in the tables represents the mean of RMSE and nRMSE of I-V curves in each dataset, while the *Std* is the standard deviation of the RMSE and nRMSE of I-V curves. As shown in Tables 7–12, the datasets for different methods are identical, so as to make the fair comparison. It can be seen in the Table 7 that there is no validation dataset for the white-box method, because the white-box method is not kind of machine learning algorithms.

Firstly, the equivalent circuit based white-box method is compared with the black-box methods on the xSi11246 PV module. As shown in Table 7, it can be seen that the error statistical results of the white-box method are one or two orders of magnitude higher than that of black-box methods, in terms of the training and testing errors. Therefore, the white-box model is not comparable to the black-box models, and thus it is not further examined on other PV modules. Secondly, the four black-box methods are further compared on the six different types of PV modules, and the corresponding results are given in Tables 7–12 where

the best results are marked in bold. It can be seen that the datasets are divided into three independent datasets, including the training set, validation set and test set. The training set is used to iteratively train the regression model, while the validation set is used to stop the iteration and/or optimize the model parameters. For the white-box model, there is not validation set, because it only uses curve fitting techniques without a learning algorithm. Both of the training set and validation sets can be used to quantify the training accuracy. The test dataset is not involved in the model training and can be regarded as unknown new data samples. Therefore, the test dataset can be used to quantify the generalization performance of the established model. From Tables 7–12, we can see that the statistical result of the proposed 1-D ResNet is basically in the order of 1E-3 and is one or two orders of magnitude less than other conventional ANN based models. Therefore, the proposed 1-D ResNet based black-box model demonstrates obvious superiority to other three conventional ANN based models on the three datasets for all the six PV modules, in terms of accuracy, generalization performance and reliability. Among the three conventional ANN, the MLP shows better performance than ELM and GRNN, but it is clearly worse than the proposed 1-D ResNet based model.

In addition, the proposed 1-D ResNet based model is further compared with the best conventional ANN MLP directly on simulated I-V curves. As shown in Figs. 17–22, six I-V curves of different operating conditions are selected from the test datasets of the six PV modules, which are used to illustrate the performance of the two models at various operating irradiance and temperature. The range of the solar

**Table 8**

Comparison of the black-box models on mSi0251.

Algorithm	Process	Amount	RMSE		nRMSE	
			Mean	Std	Mean	Std
ELM	Training set	5214	1.619E−02	1.280E−02	7.460E−02	1.236E−01
	Validation set	591	1.842E−02	1.788E−02	7.984E−02	1.436E−01
	Test set	2478	2.056E−02	9.479E−02	1.014E−01	6.325E−01
MLP	Training set	5214	8.534E−03	7.117E−03	2.660E−02	2.785E−02
	Validation set	591	8.734E−03	7.191E−03	2.551E−02	2.579E−02
	Test set	2478	8.811E−03	7.635E−03	2.688E−02	2.782E−02
GRNN	Training set	5214	1.406E−02	1.068E−02	5.701E−02	7.838E−02
	Validation set	591	2.901E−02	2.874E−02	1.051E−01	2.195E−01
	Test set	2478	3.043E−02	3.760E−02	1.137E−01	2.238E−01
1-D ResNet	Training set	5214	<b>2.170E−03</b>	<b>8.034E−04</b>	<b>9.024E−03</b>	<b>1.101E−02</b>
	Validation set	591	<b>2.318E−03</b>	<b>1.216E−03</b>	<b>9.697E−03</b>	<b>1.472E−02</b>
	Test set	2478	<b>2.305E−03</b>	<b>1.906E−03</b>	<b>9.584E−03</b>	<b>2.364E−02</b>

**Table 9**

Comparison of the black-box models on CdTe75669.

Algorithm	Process	Amount	RMSE		nRMSE	
			Mean	Std	Mean	Std
ELM	Training set	5251	1.082E−01	9.411E−02	6.670E−01	1.042E−00
	Validation set	597	1.059E−01	9.168E−02	5.888E−01	8.619E−01
	Test set	2500	2.214E−01	5.681E−01	1.435E+01	6.846E+02
MLP	Training set	5251	1.978E−02	1.098E−02	1.274E−01	2.073E−01
	Validation set	597	1.951E−02	1.025E−02	1.167E−01	1.682E−01
	Test set	2500	1.978E−02	1.141E−02	1.313E−01	4.009E−01
GRNN	Training set	5251	1.101E−02	9.477E−03	5.369E−02	6.663E−02
	Validation set	597	2.661E−02	3.303E−02	1.179E−01	1.499E−01
	Test set	2500	2.522E−02	3.258E−02	1.205E−01	1.821E−01
1-D ResNet	Training set	5251	1.945E−03	1.140E−03	1.030E−02	1.202E−02
	Validation set	597	2.063E−03	1.290E−03	1.044E−02	1.164E−02
	Test set	2500	2.200E−03	2.584E−03	1.619E−02	2.355E−01

**Table 10**

Comparison of the black-box models on CIGS1-001.

Algorithm	Process	Amount	RMSE		nRMSE	
			Mean	Std	Mean	Std
ELM	Training set	5254	4.827E−02	4.046E−02	1.162E−01	1.972E−01
	Validation set	600	5.061E−02	4.986E−02	1.333E−01	3.496E−01
	Test set	2506	5.254E−02	1.031E−01	1.530E−01	8.526E−01
MLP	Training set	5254	1.432E−02	1.158E−02	1.924E−02	1.229E−02
	Validation set	600	1.436E−02	1.108E−02	1.954E−02	1.207E−02
	Test set	2506	1.440E−02	1.139E−02	1.945E−02	1.230E−02
GRNN	Training set	5254	1.226E−02	9.704E−03	2.616E−02	3.379E−02
	Validation set	600	4.526E−02	6.160E−02	8.339E−02	1.223E−01
	Test set	2506	4.182E−02	5.111E−02	7.775E−02	1.044E−01
1-D ResNet	Training set	5254	2.988E−03	1.496E−03	5.851E−03	5.397E−03
	Validation set	600	3.350E−03	1.855E−03	6.628E−03	7.297E−03
	Test set	2506	3.290E−03	1.736E−03	6.403E−03	6.580E−03

**Table 11**

Comparison of the black-box models on HIT05662.

Algorithm	Process	Amount	RMSE		nRMSE	
			Mean	Std	Mean	Std
ELM	Training set	5238	1.575E−01	1.264E−01	3.128E−01	5.819E−01
	Validation set	597	1.598E−01	1.333E−01	3.115E−01	6.145E−01
	Test set	2492	1.573E−01	1.327E−01	3.259E−01	7.558E−01
MLP	Training set	5238	3.442E−02	2.602E−02	3.238E−02	2.771E−02
	Validation set	597	3.545E−02	2.565E−02	3.291E−02	2.345E−02
	Test set	2492	3.475E−02	2.580E−02	3.413E−02	4.250E−02
GRNN	Training set	5238	2.899E−02	2.046E−02	4.914E−02	8.398E−02
	Validation set	597	6.333E−02	7.422E−02	8.339E−02	1.479E−01
	Test set	2492	6.122E−02	6.584E−02	8.702E−02	1.405E−01
1-D ResNet	Training set	5238	5.430E−03	2.368E−03	8.507E−03	1.145E−02
	Validation set	597	5.852E−03	2.913E−03	8.590E−03	1.042E−02
	Test set	2492	5.849E−03	2.741E−03	9.215E−03	1.467E−02

irradiance and ambient temperature are 92.9 W/m<sup>2</sup>–999.9 W/m<sup>2</sup> and 7.6–38.1 °C respectively. From these figures, it can be observed that the I-V curves simulated by our proposed 1-D ResNet based model are highly in accordance with the measured ones at different conditions on all the six PV modules. However, the I-V curves simulated by the MLP based model obviously deviate from the measured at some conditions on the PV modules CdTe75669 and aSiMicro03038. Therefore, the proposed 1-D ResNet based model are appropriate for different types of PV modules and various ranges of operating conditions.

## 5. Conclusions

Accurate and reliable modeling of DC-side PV modules/arrays is important for optimal design, operation and evaluation of PV systems. In this study, we investigate and propose two types of modeling approaches for PV modules/arrays: white-box modeling and black-box modeling. The proposed white-box modeling mainly consists of two steps of parameters extraction using the EHA-NMS hybrid optimization algorithm. The first step is to extract the five OPC parameters of single-diode model, and the second step is to extract five STC parameters and

**Table 12**

Comparison of the black-box models on aSiMicro03038.

Algorithm	Process	Amount	RMSE		nRMSE	
			Mean	Std	Mean	Std
ELM	Training set	4579	1.432E−01	9.614E−02	1.423E−00	2.469E−00
	Validation set	525	1.446E−01	1.010E−01	1.335E−00	2.180E−00
	Test set	2182	1.439E−01	1.054E−01	1.363E−00	2.240E−00
MLP	Training set	4579	1.076E−02	7.034E−03	1.039E−01	2.253E−01
	Validation set	525	1.090E−02	7.063E−03	1.002E−01	1.607E−01
	Test set	2182	1.078E−02	7.034E−03	1.025E−01	1.968E−01
GRNN	Training set	4579	1.017E−02	1.013E−02	6.516E−02	8.340E−02
	Validation set	525	3.601E−02	3.863E−02	2.123E−01	2.355E−01
	Test set	2182	3.524E−02	3.833E−02	2.091E−01	2.712E−01
1-D ResNet	Training set	4579	1.905E−03	1.266E−03	1.294E−02	1.483E−02
	Validation set	525	2.166E−03	1.480E−03	1.431E−02	1.646E−02
	Test set	2182	2.187E−03	1.595E−03	1.442E−02	1.610E−02

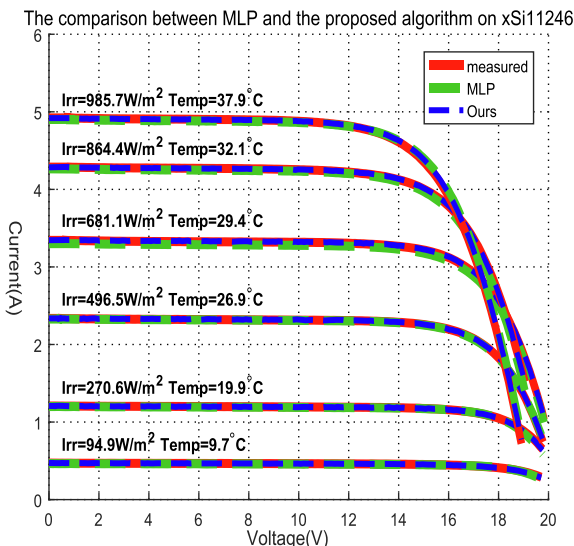


Fig. 17. Comparison between simulated and measured I-V curves of xSi11246.

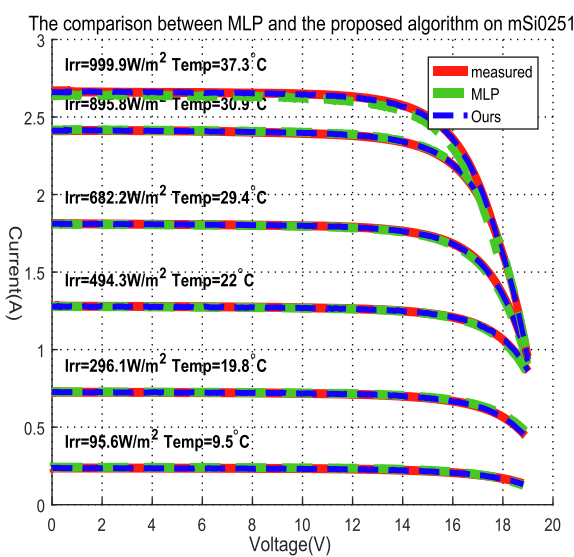


Fig. 18. Comparison between simulated and measured I-V curves of mSi0251.

two temperature coefficients from the five OPC-STC translation equations. The proposed black-box modeling method is based on a new efficient 1-D ResNet that features strong feature extraction and non-linear

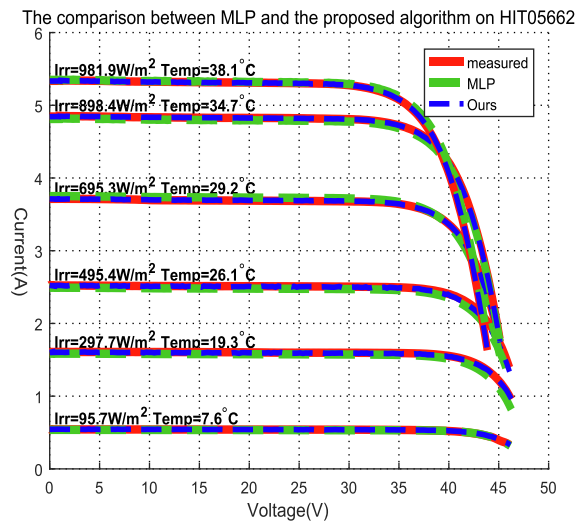


Fig. 19. Comparison between simulated and measured I-V curves of HIT05662.

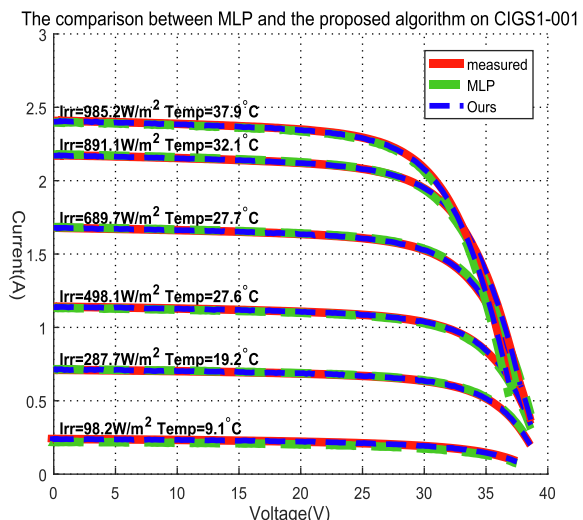


Fig. 20. Comparison between simulated and measured I-V curves of CIGS1-001.

mapping capability, which can predict a whole I-V curve at arbitrary operating conditions. The two approaches are verified using experimental I-V curves datasets of six different types of PV modules provided by NREL (identifiers: xSi11246, mSi0251, CdTe75669, CIGS1-001, HIT05662 and aSiMicro03038). To improve the modeling efficiency,

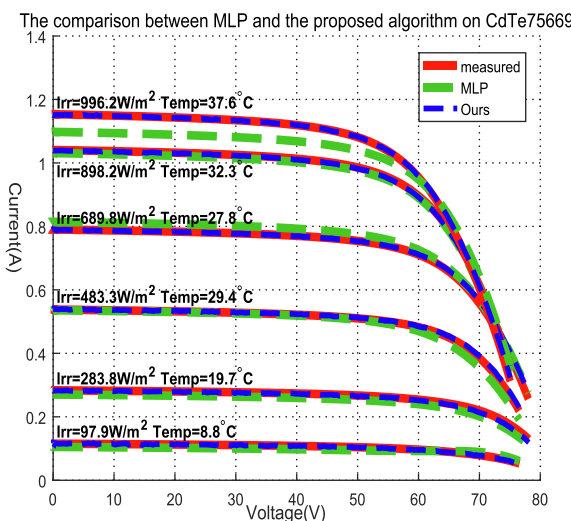


Fig. 21. Comparison between simulated and measured I-V curves of CdTe75669.

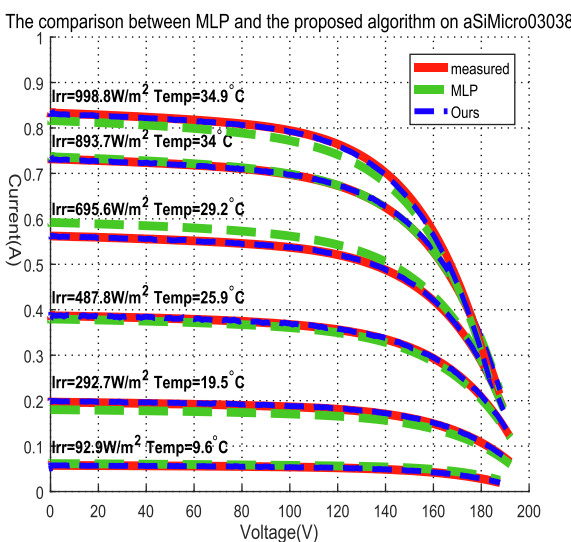


Fig. 22. Comparison between simulated and measured I-V curves of aSiMicro03038.

the original I-V curves that contain more than 175 data point are downsampled to be of 50 data points using a fixed voltage vector. In addition, in view of that the operating conditions of original I-V curves are highly non-uniform, a grid sampling method is proposed to select part of the I-V curves that features relatively uniform operating conditions for training and testing the PV models, so as to improve the generalization performance.

The proposed white-box modeling and 1-D ResNet based modeling are firstly compared on the dataset of the xSi11246 module. Experimental results show that, both on the training and testing datasets, the statistical mean and stand deviation values of I-V curve RMSE and nRMSE of the white-box model are on the order of 1E−1, while those of the black-box models are on the order of 1E−2 or 1E−3, which demonstrated that the black-box models are generally better than the white-box method. Furthermore, the 1-D ResNet based model is compared with three other conventional ANN based models (including the GRNN, ELM and MLP) on the six types of PV modules. The experimental results on the six PV modules all indicate that, for all the three datasets (training, validation and test datasets), the statistical mean and standard deviation values of I-V curve RMSE and nRMSE of the 1-D ResNet based black-box model are on the order of 1E−3 or

1E−2, while those of other three black-box models are basically on the order of 1E−2 or 1E−1.

Therefore, the black-box modeling methods are generally better than the white-box modeling method, and the proposed 1-D ResNet based black-box PV modeling is obviously superior to other investigated black-box modeling methods, in terms of accuracy, generalization performance and reliability.

## Acknowledgments

The authors would like to acknowledge the financial supports by the National Natural Science Foundation of China (Grant Nos. 61601127 and 61574038), the Fujian Provincial Department of Science and Technology of China (Grant Nos. 2016H6012 and 2018J01774), and the Fujian Provincial Department of Education of China (Grant No. JAT160073).

In addition, the authors would like to thank the National Renewable Energy Laboratory (NREL) for generously providing large datasets of experimental I-V curves of different types of PV modules, which enables the validation of the proposed PV modeling method.

## Declaration of interest

None.

## References

- PVPS, "Snapshot of Global Photovoltaic Markets 2017," Report IEAPVPS, 2017.
- Chin VJ, et al. Cell modelling and model parameters estimation techniques for photovoltaic simulator application: a review. *Appl Energy* 2015;154:500–19.
- Almonacid F, et al. Review of techniques based on artificial neural networks for the electrical characterization of concentrator photovoltaic technology. *Renewable Sustainable Energy Rev* 2017;75:938–53.
- Ram JP, et al. Analysis on solar PV emulators: a review. *Renewable Sustainable Energy Rev* 2018;81:149–60.
- Ram JP, et al. A comprehensive review on solar PV maximum power point tracking techniques. *Renewable Sustainable Energy Rev* 2017;67:826–47.
- Das UK, et al. Forecasting of photovoltaic power generation and model optimization: a review. *Renewable Sustainable Energy Rev* 2018;81:912–28.
- Chen Z, et al. Intelligent fault diagnosis of photovoltaic arrays based on optimized kernel extreme learning machine and IV characteristics. *Appl Energy* 2017;204:912–31.
- Garoudia E, et al. An enhanced machine learning based approach for failures detection and diagnosis of PV systems. *Energy Convers Manage* 2017;151:496–513.
- Chen Z, et al. Random forest based intelligent fault diagnosis for PV arrays using array voltage and string currents. *Energy Convers Manage* 2018;178:250–64.
- Pillai DS, Rajasekar N. A comprehensive review on protection challenges and fault diagnosis in PV systems. *Renewable Sustainable Energy Rev* 2018;91:18–40.
- Dhimish M, et al. Photovoltaic fault detection algorithm based on theoretical curves modelling and fuzzy classification system. *Energy* 2017;140:276–90.
- Cuce E, et al. An accurate model for photovoltaic (PV) modules to determine electrical characteristics and thermodynamic performance parameters. *Energy Convers Manage* 2017;146:205–16.
- Ma T, et al. Development of a model to simulate the performance characteristics of crystalline silicon photovoltaic modules/strings/arrays. *Sol Energy* 2014;100:31–41.
- Ma T, et al. Solar photovoltaic system modeling and performance prediction. *Renewable Sustainable Energy Rev* 2014;36:304–15.
- Ma T, et al. Performance evaluation of a stand-alone photovoltaic system on an isolated island in Hong Kong. *Appl Energy* 2013;112:663–72.
- Chin VJ, et al. An accurate modelling of the two-diode model of PV module using a hybrid solution based on differential evolution. *Energy Convers Manage* 2016;124:42–50.
- Mahmoud Y, El-Saadany EF. A photovoltaic model with reduced computational time. *IEEE Trans Ind Electron* 2015;62:3534–44.
- Elbaset AA, et al. New seven parameters model for amorphous silicon and thin film PV modules based on solar irradiance. *Sol Energy* 2016;138:26–35.
- Yahya-Khotbehsara A, Shahhoseini A. A fast modeling of the double-diode model for PV modules using combined analytical and numerical approach. *Sol Energy* 2018;162:403–9.
- Mellit A, et al. Modeling and simulation of a stand-alone photovoltaic system using an adaptive artificial neural network: Proposition for a new sizing procedure. *Renewable Energy* 2007;32:285–313.
- Zhu H, et al. Online modelling and calculation for operating temperature of silicon-based PV modules based on BP-ANN. *Int J Photoenergy* 2017;2017:1–13.
- Nunes HGG, et al. A new high performance method for determining the parameters of PV cells and modules based on guaranteed convergence particle swarm

- optimization. *Appl Energy* 2018;211:774–91.
- [23] Gao X, et al. Parameter extraction of solar cell models using improved shuffled complex evolution algorithm. *Energy Convers Manage* 2018;157:460–79.
- [24] Chen Y, et al. An improved explicit double-diode model of solar cells: Fitness verification and parameter extraction. *Energy Convers Manage* 2018;169:345–58.
- [25] Piazza MCD, et al. Dynamic PV model parameter identification by least-squares regression. *IEEE J Photovoltaics* 2013;3:799–806.
- [26] Lopez-Gude JM, et al. Electrical behavior modeling of solar panels using extreme learning machines. Presented at the International Conference on Hybrid Artificial Intelligence Systems. Springer; 2018.
- [27] Wolf P, Benda V. Identification of PV solar cells and modules parameters by combining statistical and analytical methods. *Sol Energy* 2013;93:151–7.
- [28] Kim KA, et al. A dynamic photovoltaic model incorporating capacitive and reverse-bias characteristics. *IEEE J Photovoltaics* 2013;3:1334–41.
- [29] Pillai DS, Rajasekar N. Metaheuristic algorithms for PV parameter identification: a comprehensive review with an application to threshold setting for fault detection in PV systems. *Renewable Sustainable Energy Rev* 2017.
- [30] Jordhei AR. Parameter estimation of solar photovoltaic (PV) cells: a review. *Renewable Sustainable Energy Rev* 2016;61:354–71.
- [31] Orioli A, Di Gangi A. A procedure to calculate the five-parameter model of crystalline silicon photovoltaic modules on the basis of the tabular performance data. *Appl Energy* 2013;102:1160–77.
- [32] Bai J, et al. Development of a new compound method to extract the five parameters of PV modules. *Energy Convers Manage* 2014;79:294–303.
- [33] Wu L, et al. Parameter extraction of photovoltaic models from measured I-V characteristics curves using a hybrid trust-region reflective algorithm. *Appl Energy* 2018;232C:36–53.
- [34] Xiong G, et al. Parameter extraction of solar photovoltaic models using an improved whale optimization algorithm. *Energy Convers Manage* 2018;174:388–405.
- [35] Chin VJ, et al. An accurate and fast computational algorithm for the two-diode model of PV module based on a hybrid method. *IEEE Trans Ind Electron* 2017;64:6212–22.
- [36] Toledo FJ, et al. Two-step linear least-squares method for photovoltaic single-diode model parameters extraction. *IEEE Trans Ind Electron* 2018.
- [37] Soon JJ, Low KS. Photovoltaic model identification using particle swarm optimization with inverse barrier constraint. *IEEE Trans Power Electron* 2012;27:3975–83.
- [38] Castro R. Data-driven PV modules modelling: comparison between equivalent electric circuit and artificial intelligence based models. *Sustainable Energy Technol Assess* 2018;30:230–8.
- [39] Askarzadeh A. Voltage prediction of a photovoltaic module using artificial neural networks. *Int Trans Electric Energy Syst* 2015;24:1715–25.
- [40] Almonacid F, et al. High concentrator photovoltaic module simulation by neuronal networks using spectrally corrected direct normal irradiance and cell temperature. *Energy* 2015;84:336–43.
- [41] Zarate LE, et al. Artificial neural networks applied for representation of curves current-voltage of photovoltaic modules. *IEEE Int Conf Ind Inf* 2008;1644–9.
- [42] Celik AN. Artificial neural network modelling and experimental verification of the operating current of mono-crystalline photovoltaic modules. *Sol Energy* 2011;85:2507–17.
- [43] Khatib T, et al. A new offline method for extracting IV characteristic curve for photovoltaic modules using artificial neural networks. *Sol Energy* 2018;173:462–9.
- [44] Bonanno F, et al. A radial basis function neural network based approach for the electrical characteristics estimation of a photovoltaic module. *Appl Energy* 2012;97:956–61.
- [45] Almonacid F, et al. Characterisation of Si-crystalline PV modules by artificial neural networks. *Renewable Energy* 2009;34:941–9.
- [46] Pilioungine M, et al. Modelling photovoltaic modules with neural networks using angle of incidence and clearness index. *Prog Photovoltaics Res Appl* 2015;23:513–23.
- [47] Almonacid F, et al. Characterisation of PV CIS module by artificial neural networks. a comparative study with other methods. *Renewable Energy* 2010;35:973–80.
- [48] Pilioungine M, et al. Photovoltaic module simulation by neural networks using solar spectral distribution. *Prog Photovoltaics Res Appl* 2013;21:1222–35.
- [49] Lopez-Gude JM, et al. Electrical Behavior Modeling of Solar Panels Using Extreme Learning Machines. *Int Conf Hybrid Artif Intell Syst* 2018:730–40.
- [50] Schmidhuber J. Deep learning in neural networks: an overview. *Neural networks* 2015;61:85–117.
- [51] Wang H, et al. Deterministic and probabilistic forecasting of photovoltaic power based on deep convolutional neural network. *Energy Convers Manage* 2017;153:409–22.
- [52] Liu W, et al. A survey of deep neural network architectures and their applications. *Neurocomputing* 2017;234:11–26.
- [53] He K, et al. “Deep residual learning for image recognition.” In: Proceedings of the IEEE conference on computer vision and pattern recognition; 2016, pp. 770–78.
- [54] Sabry YH, et al. Measurement-based modeling of a semitransparent CdTe thin-film PV module based on a custom neural network. *IEEE Access* 2018;6:34934–47.
- [55] Mellit A, et al. Artificial neural network-based model for estimating the produced power of a photovoltaic module. *Renewable Energy* 2013;60:71–8.
- [56] Garcia-Domingo B, et al. CPV module electric characterisation by artificial neural networks. *Renewable Energy* 2015;78:173–81.
- [57] Pilioungine M, et al. Multilayer perceptron applied to the estimation of the influence of the solar spectral distribution on thin-film photovoltaic modules. *Appl Energy* 2013;112:610–7.
- [58] Marion B, et al. New data set for validating PV module performance models. *Photovoltaic Specialist Conference (PVSC), 2014 IEEE 40th. IEEE*, 2014. p. 1362–6.
- [59] Chen Z, et al. Parameters identification of photovoltaic models using hybrid adaptive Nelder-Mead simplex algorithm based on eagle strategy. *Appl Energy* 2016;182:47–57.
- [60] Ince T, et al. Real-time motor fault detection by 1-D convolutional neural networks. *IEEE Trans Ind Electron* 2016;63(11):7067–75.
- [61] Abdeljaber O, et al. Real-time vibration-based structural damage detection using one-dimensional convolutional neural networks. *J Sound Vib* 2017;388:154–70.
- [62] He K, et al. “Deep Residual Learning for Image Recognition.” In: Presented at the 2016 IEEE Conference on Computer Vision and Pattern Recognition (CVPR), Las Vegas, NV, United States, 2015.
- [63] Ioffe S, Szegedy C. “Batch Normalization: Accelerating Deep Network Training by Reducing Internal Covariate Shift.” In: Presented at the Proceedings of the 32nd International Conference on International Conference on Machine Learning – Volume 37, Lille, France, 2015.
- [64] He K, et al. Identity mappings in deep residual networks. *Cham* 2016:630–45.
- [65] Rumelhart DE, et al. Learning representations by back-propagating errors vol. 323: MIT Press; 1986.
- [66] Sutskever I, et al. “On the importance of initialization and momentum in deep learning.” In: International Conference on International Conference on Machine Learning, 2013, pp. III-1139.
- [67] Duchi J, et al. Adaptive subgradient methods for online learning and stochastic optimization. *J Mach Learn Res* 2011;12:257–69.
- [68] Tieleman TAH, G. “Lecture 6.5 - RMSProp, COURSERA: Neural Networks for Machine Learning.” Technical report; 2012.
- [69] Kingma DP, Ba J. Adam: a method for stochastic optimization. *Comput Sci* 2014.
- [70] Glorot X, Bengio Y. Understanding the difficulty of training deep feedforward neural networks. *J Mach Learn Res* 2010;9:249–56.
- [71] Hinton GE, et al. Improving neural networks by preventing co-adaptation of feature detectors. *Comput Sci* 2012;3:212–23.
- [72] Duan QY, et al. Shuffled complex evolution approach for effective and efficient global minimization. *J Optim Theory Appl* 1993;76:501–21.